

Immersogeometric Analysis of Bioprosthetic Heart Valves, Using the Dynamic Augmented Lagrangian Method



Ming-Chen Hsu and David Kamensky

Abstract In the mid-2010s, we began applying a combination of isogeometric analysis and immersed boundary methods to the problem of bioprosthetic heart valve (BHV) fluid–structure interaction (FSI). This chapter reviews how our research on BHV FSI (1) crystallized the emerging concept of *immersogeometric analysis*, (2) introduced a new semi-implicit numerical method for weakly enforcing constraints in time dependent problems, which we refer to as the *dynamic augmented Lagrangian* approach, and (3) clarified the important role of mass conservation in immersed FSI analysis. We illustrate these contributions with selected numerical results and discuss future improvements to, and applications of, the computational FSI techniques we have developed.

1 Introduction

Heart valves are passive anatomical structures driven by hemodynamic forces. They ensure proper unidirectional blood flow through the heart. At least 280,000 diseased valves are replaced annually [1, 2]. The most popular replacements are bioprosthetic heart valves (BHV), fabricated from biologically derived materials [3]. Like native valves, BHVs consist of flexible leaflets. BHVs have more natural hemodynamics than the older “mechanical” prosthesis designs, which consist of rigid moving parts [2]. However, the lifespans of typical BHVs remain limited to ~ 10 –15 years, with structural deterioration mediated by fatigue and tissue mineralization [1, 2, 4, 5]. Much research has sought to prevent mineralization, but methods to

M.-C. Hsu (✉)

Department of Mechanical Engineering, Iowa State University, Ames, IA, USA

e-mail: jmchsu@iastate.edu

D. Kamensky

Department of Structural Engineering, University of California, San Diego, La Jolla, CA, USA

e-mail: dmkamensky@eng.ucsd.edu

© Springer Nature Switzerland AG 2018

T. E. Tezduyar (ed.), *Frontiers in Computational Fluid-Structure Interaction and Flow Simulation*, Modeling and Simulation in Science, Engineering and Technology, https://doi.org/10.1007/978-3-319-96469-0_5

167

extend durability remain less explored. Central to such efforts is an understanding of the stresses in BHV leaflets over the cardiac cycle.

Computational methods may be used for stress analysis of heart valves. Some previous computational studies on heart valve mechanics used (quasi-)static [6, 7] and dynamic [8] structural analysis, with assumed pressure loads. However, pure structural analysis is only accurate for static pressurization of a closed valve, which represents just part of the full cardiac cycle. It is therefore important to simulate the dynamics of heart valves interacting with blood, using computational fluid–structure interaction (FSI).

1.1 Computational FSI Analysis of Heart Valves

Heart valves present several challenges for FSI analysis. Most notably, the valve leaflets contact one another, changing the fluid subdomain’s topology. This section updates the literature review of [3] to cover some additional recent work. Standard arbitrary Lagrangian–Eulerian (ALE) [9–11] or deforming-spatial-domain/space–time (DSD/ST) [12, 13] formulations, which continuously deform the fluid domain from some reference configuration, are no longer directly applicable. One must augment these methods with special techniques to handle extreme deformations. One solution is to generate a new mesh of finite elements or volumes for the fluid domain whenever its deformation becomes too extreme [14–17]. This allows computations to proceed, but introduces additional computational cost and numerical errors. Some recent work by Takizawa and collaborators [18] introduced a novel space–time with topology change (ST-TC) method that permits topology change without re-meshing. Takizawa et al. [19] applied the ST-TC approach to CFD analysis of a heart valve, and later extended the approach to include sliding interfaces in [20, 21], rendering it suitable for future full FSI analysis.

In light of the aforementioned difficulties, the majority of work to-date on heart valve FSI analysis has invoked Peskin’s immersed boundary concept [22]. While it is not a universal convention, we follow [23–25] in applying the term “immersed boundary method” broadly, to describe any numerical method for approximating partial differential equations (PDEs) that allows boundaries of the PDE domain to cut arbitrarily through a computational mesh. Researchers may have varying interpretations of the term “immersed boundary method,” and we recommend that writers clarify its meaning within a particular document.

Immersed boundary methods for FSI greatly simplify treatment of large structural deformations, but engender several disadvantages relative to ALE and DSD/ST techniques [26]. In particular, they struggle to efficiently capture boundary layer solutions near fluid–structure interfaces. Takizawa et al. [27] found that resolving such layers is essential to obtaining accurate shear stresses in hemodynamic analysis. A comprehensive overview of various immersed boundary methods and their properties is beyond the scope of this literature review; we refer the interested reader to [23, 24].

Peskin introduced the immersed boundary concept specifically to meet the demands of heart valve FSI analysis [22]. The numerical method proposed by

Peskin has found little if any direct application by bioengineers, though, due to its crude representation of the heart valve as a collection of markers connected by elastic fibers. However, deficient modeling of the structure subproblem is not an inherent feature of immersed boundary methods. In the early 2000s, [28–33] used an immersed boundary method introduced in [34] to couple finite element discretizations of heart valves and blood flow. This allowed investigation of various constitutive models, but numerical instabilities prevented analysis at realistic Reynolds numbers and transvalvular pressures. Increasing availability of parallel computing resources in the 2010s led to higher resolution simulations of heart valves. Griffith [35] adapted Peskin’s original method to modern distributed-memory computer architectures and included adaptive mesh refinement for the fluid subproblem, to compute FSI of a native aortic valve throughout a full cardiac cycle, with physiological flow velocities and pressure differences. Borazjani [36] applied the curvilinear immersed boundary (CURVIB) method [37, 38] to simulate systolic ejection through a bioprosthetic aortic valve, using nearly 10 million grid points in the fluid domain. The valve leaflet models in the studies by Griffith and Borazjani suffered from deficiencies, though, with [35] modeling the leaflets in the style of Peskin, as markers connected by elastic fibers, and [36] omitting bending stiffness. The CURVIB method was recently extended to include fluid–shell structure interaction in [39, 40].

The immersed analyses cited above relied on academic research codes. As early as the late 1990s, immersed methods in the commercial software LS-DYNA [41] were used for FSI simulations of bioprosthetic and native aortic valves [42–45]. The time-explicit procedures used by LS-DYNA result in severe Courant–Friedrichs–Lewy conditions [46, 47], limiting stable time step size in hemodynamic computations, because blood is nearly incompressible. References [44, 45] circumvented this difficulty by artificially reducing the sound speed by a significant factor, reporting that the fluid density variations introduced by this deliberate modeling error were negligible. Other commercial analysis software for heart valve FSI analysis may be usable through “black box” coupling algorithms [48] that connect independent finite element analysis and CFD programs without access to their internal details. Specialized methods are required for stable and efficient black box coupling of fluids to thin, light structures such as heart valve leaflets [49, 50]. Astorino et al. [51] applied a novel black box coupling algorithm to FSI analysis of an idealized aortic valve. Remeshing functionality in ANSYS software has also recently allowed for boundary-fitted simulations of heart valves [52].

1.2 Immersogeometric Analysis

Following the majority of the studies cited in Sect. 1.1, our own work has employed an immersed approach to heart valve FSI analysis. The goal of immersed methods has always been to simplify the construction of analysis-suitable computational models from available geometric data specifying the domain of a PDE system. Traditional immersed boundary analysis eases this process by allowing subproblems to be discretized separately, then coupled through a numerical method.

Another technology for simplifying computational model generation is isogeometric analysis (IGA) [53]. IGA is based on the insight that many geometries in engineering design are specified in spline spaces that can be enriched, then used to approximate PDE solutions. These spline spaces also have desirable mathematical properties, including control over smoothness, improved approximation power [54], and straightforward constructions of discrete de Rham complexes [55, 56]. Benefits of these properties are evident in fluid and structural analyses, including studies of incompressible flow [57–60], thin shells [61–64], extreme mesh distortion [65], and contact [66, 67]. IGA encounters difficulties, though, when faced with realistic engineering designs. Foremost among these are:

1. Many designs of volumes are specified in terms of bounding spline surfaces. If analysts wish to solve PDEs in such volumes, then IGA, as originally conceived, is inapplicable.
2. Spline surfaces in designs are frequently trimmed along curves that do not conform to the parametric supports of the spline space's basis functions. The analysis space suggested by standard IGA is therefore not fitted to the boundaries of the PDE domain.

These challenges could be addressed by changing the way in which engineering products are designed: designers could transition to geometry representations that are analysis-suitable. Changing the habits of designers throughout industry, though, would require an incredible feat of mass persuasion. Undeterred, creators of analysis-suitable design technologies (e.g., [68–70]) have succeeded at incorporating their work into some major commercial design platforms. It remains doubtful, though, that analysis-suitable design will become standard any time soon. Further, many designs specified in past formats will remain relevant long into the future.

One way to make IGA practical without changing the design process is to incorporate immersed boundary methods. Difficulty 1 can be alleviated by creating a convenient unfitted analysis space covering the volume of interest, then using an immersed boundary method to enforce the desired boundary conditions on the spline surfaces. Difficulty 2 can be addressed by using the natural isogeometric solution space, and treating the trim curves as immersed boundaries. Promising work in both of these directions has been carried out using an immersed boundary approach called the finite cell method [71–75]. In addition to patching weaknesses of IGA, direct application of immersed boundary techniques to design geometries can eliminate the meshing and consequent geometrical approximation¹ from traditional immersed boundary analysis. In [77], we introduced the term *immersogeometric analysis* (IMGA) to describe this symbiotic union of immersed boundary and isogeometric technologies.²

¹In practice, immersogeometric methods must frequently approximate integrals over the domain geometry, which may be considered a type of geometrical approximation [76, Sections 4.3 and 4.4], but this is conceptually distinct from the direct alteration of domain geometry that occurs in traditional mesh generation.

²The word “immersogeometric” was originally coined in 2014 by T. J. R. Hughes, while traveling in Italy; it is derived from the Italian word *immerso*, meaning “immersed.”

1.3 Structure and Content of This Chapter

Section 2 states the coupled PDEs that we use to model the FSI system. Section 3 describes the isogeometric spatial discretizations for the fluid and structure subproblems. Section 4 completes the discretization with a semi-implicit coupling scheme that we call the *dynamic augmented Lagrangian* (DAL) method. Section 5 demonstrates the accuracy of the proposed methods, looking at both norm convergence and quantities of interest in nonlinear benchmark problems. Section 6 applies DAL-based IMGA to BHV FSI simulation and compares the results to in vitro experimental work. Finally, Sect. 7 sketches some future developments that may improve on the technology described in this chapter, connect it to clinical practice, and apply it to other FSI problems.

2 Mathematical Model of FSI

We model BHV leaflets as Kirchhoff–Love thin shells. We model the surrounding fluid as incompressible and Newtonian. The subproblems are coupled through kinematic and dynamic conditions on the fluid–solid interface. The thin structure is modeled geometrically as a 2D surface embedded in the 3D fluid domain. We state the model in a weak form, which is both suggestive of finite-dimensional approximations and conducive to including distributional forces from immersed boundaries.

Remark 1 We do not include a condition that the structure cannot intersect itself. Inclusion of such a constraint would be redundant in light of FSI kinematics, since a continuous velocity field is defined throughout the fluid–structure continuum [78]. While it is, in practice, useful to include some specialized treatment of structure-on-structure contact in a numerical method, we consider that a feature of the discretization, not the mathematical model.

2.1 Augmented Lagrangian Formulation of FSI

We start from the augmented Lagrangian framework for FSI introduced by Bazilevs et al. [79], and specialize to the case of thin structures. The region occupied by fluid at time t is $(\Omega_1)_t \subset \mathbb{R}^d$. The structure geometry at time t is modeled by the hypersurface $\Gamma_t \subset (\Omega_1)_t$. Let \mathbf{u}_1 denote the fluid’s velocity and p denote its pressure. Let \mathbf{y} denote the structure’s displacement from some reference configuration, Γ_0 , and $\mathbf{u}_2 \equiv \dot{\mathbf{y}}$ denote the velocity of the structure. The fluid–structure kinematic constraint, $\mathbf{u}_1 = \mathbf{u}_2$ on Γ_t , is enforced by the augmented Lagrangian

$$\int_{\Gamma_t} \lambda \cdot (\mathbf{u}_1 - \mathbf{u}_2) \, d\Gamma + \frac{1}{2} \int_{\Gamma_t} \beta |\mathbf{u}_1 - \mathbf{u}_2|^2 \, d\Gamma, \quad (1)$$

where λ is a Lagrange multiplier and $\beta \geq 0$ is a penalty parameter. The resulting variational problem is: Find $\mathbf{u}_1 \in \mathcal{S}_u$, $p \in \mathcal{S}_p$, $\mathbf{y} \in \mathcal{S}_d$, and $\lambda \in \mathcal{S}_\ell$ such that, for all test functions $\mathbf{w}_1 \in \mathcal{V}_u$, $q \in \mathcal{V}_p$, $\mathbf{w}_2 \in \mathcal{V}_d$, and $\delta\lambda \in \mathcal{V}_\ell$

$$B_1(\{\mathbf{u}_1, p\}, \{\mathbf{w}_1, q\}; \hat{\mathbf{u}}) - F_1(\{\mathbf{w}_1, q\}) + \int_{\Gamma_i} \mathbf{w}_1 \cdot \lambda \, d\Gamma + \int_{\Gamma_i} \mathbf{w}_1 \cdot \beta(\mathbf{u}_1 - \mathbf{u}_2) \, d\Gamma = 0, \quad (2)$$

$$B_2(\mathbf{y}, \mathbf{w}_2) - F_2(\mathbf{w}_2) - \int_{\Gamma_i} \mathbf{w}_2 \cdot \lambda \, d\Gamma - \int_{\Gamma_i} \mathbf{w}_2 \cdot \beta(\mathbf{u}_1 - \mathbf{u}_2) \, d\Gamma = 0, \quad (3)$$

$$\int_{\Gamma_i} \delta\lambda \cdot (\mathbf{u}_1 - \mathbf{u}_2) \, d\Gamma = 0, \quad (4)$$

where \mathcal{S}_u , \mathcal{S}_p , \mathcal{S}_d , and \mathcal{S}_ℓ are the trial solution spaces for the fluid velocity, fluid pressure, structural displacement, and interface Lagrange multiplier solutions. \mathcal{V}_u , \mathcal{V}_p , \mathcal{V}_d , and \mathcal{V}_ℓ are the corresponding test spaces. B_1 , B_2 , F_1 , and F_2 are forms defining the (weak) fluid and structure subproblems.

2.2 Fluid Subproblem

The fluid subproblem is incompressible and Newtonian:

$$B_1(\{\mathbf{u}, p\}, \{\mathbf{w}, q\}; \hat{\mathbf{u}}) = \int_{(\Omega_1)_t} \mathbf{w} \cdot \rho_1 \left(\frac{\partial \mathbf{u}}{\partial t} \Big|_{\hat{\mathbf{x}}} + (\mathbf{u} - \hat{\mathbf{u}}) \cdot \nabla \mathbf{u} \right) d\Omega + \int_{(\Omega_1)_t} \boldsymbol{\varepsilon}(\mathbf{w}) : \boldsymbol{\sigma}_1(\mathbf{u}, p) \, d\Omega + \int_{(\Omega_1)_t} q \nabla \cdot \mathbf{u} \, d\Omega - \gamma \int_{(\Gamma_{1h})_t} \mathbf{w} \cdot \rho_1 \{(\mathbf{u} - \hat{\mathbf{u}}) \cdot \mathbf{n}_1\}_- \mathbf{u} \, d\Gamma, \quad (5)$$

$$F_1(\{\mathbf{w}, q\}) = \int_{(\Omega_1)_t} \mathbf{w} \cdot \rho_1 \mathbf{f}_1 \, d\Omega + \int_{(\Gamma_{1h})_t} \mathbf{w} \cdot \mathbf{h}_1 \, d\Gamma, \quad (6)$$

where ρ_1 is the fluid mass density, $\boldsymbol{\varepsilon}$ is the symmetric gradient operator, $\boldsymbol{\sigma}_1(\mathbf{u}, p) = -p\mathbf{I} + 2\mu\boldsymbol{\varepsilon}(\mathbf{u})$, where μ is the dynamic viscosity, \mathbf{f}_1 is a prescribed body force, and \mathbf{h}_1 is a prescribed traction on $\Gamma_{1h} \subset \partial\Omega_1$. $(\Omega_1)_t$ deforms from some reference configuration, $(\Omega_1)_0$, according to the velocity field $\hat{\mathbf{u}}$, which need not equal \mathbf{u}_1 . $\partial(\cdot)/\partial t|_{\hat{\mathbf{x}}}$ indicates time differentiation with respect to a fixed point $\hat{\mathbf{x}}$ from $(\Omega_1)_0$. The last term of (5) is not usually considered to be part of the weak Navier–Stokes

problem, but it enhances the stability of the problem in cases where flow enters through the Neumann boundary $\Gamma_{1\mathbf{h}}$ [80]. The function $\{\cdot\}_-$ isolates the negative part of its argument. The coefficient $\gamma \geq 0$ controls the strength of this stabilizing term and \mathbf{n}_1 is the outward-facing normal to Ω_1 .

2.3 Thin Structure Subproblem

Following the Kirchhoff–Love thin shell kinematic hypotheses (see, e.g., [61, 62, 64]), B_2 and F_2 are defined as

$$B_2(\mathbf{y}, \mathbf{w}) = \int_{\Gamma_t} \mathbf{w} \cdot \rho_2 h_{\text{th}} \frac{\partial^2 \mathbf{y}}{\partial t^2} \Big|_{\mathbf{X}} d\Gamma + \int_{\Gamma_0} \int_{-h_{\text{th}}/2}^{h_{\text{th}}/2} D_{\mathbf{w}} \mathbf{E} : \mathbf{S} d\xi^3 d\Gamma \quad (7)$$

and

$$F_2(\mathbf{w}) = \int_{\Gamma_t} \mathbf{w} \cdot \rho_2 h_{\text{th}} \mathbf{f}_2 d\Gamma + \int_{\Gamma_t} \mathbf{w} \cdot \mathbf{h}^{\text{net}} d\Gamma, \quad (8)$$

where ρ_2 is the structure mass density, \mathbf{f}_2 is a prescribed body force, h_{th} is the thickness of the shell, ξ^3 is a through-thickness coordinate, and we have referred the elasticity term to the reference configuration. \mathbf{E} is the Green–Lagrange strain tensor [81, (2.67)] corresponding to the displacement \mathbf{y} , $D_{\mathbf{w}} \mathbf{E}$ is its functional derivative in the direction \mathbf{w} , and \mathbf{S} is the second Piola–Kirchhoff stress tensor [81, (3.63)], depending on \mathbf{E} . The last term of F_2 sums the prescribed tractions on the two sides of Γ_t . $\partial(\cdot)/\partial t|_{\mathbf{X}}$ indicates time differentiation with respect to a fixed material point. The Green–Lagrange strain \mathbf{E} is simplified to depend entirely on the shell structure’s midsurface displacement, $\mathbf{y} : \Gamma_0 \rightarrow \mathbb{R}^d$, using Kirchhoff–Love shell kinematic assumptions [61, 64], thus reducing the dimension of the PDE domain.

Any material model that accepts a Green–Lagrange strain \mathbf{E} and returns a 2nd Piola–Kirchhoff stress \mathbf{S} can be used directly in the structure subproblem defined above. In the work summarized by this chapter, we model BHV leaflets as hyperelastic, meaning that $\mathbf{S} = \partial\Psi/\partial\mathbf{E}$, where Ψ maps strains to energy densities [81, Chapter 6].

3 Discretization of Subproblems

Distinct fluid and structure subproblems may be isolated from the coupled problem stated in Sect. 2 by setting the test function corresponding to the other subproblem and the test function corresponding to the kinematic constraint to zero. Each of these subproblems may be discretized by adapting existing techniques for computational fluid and structural dynamics.

3.1 Fluid Subproblem

The fluid subproblem may be isolated by setting $\mathbf{w}_2 = \delta\boldsymbol{\lambda} = \mathbf{0}$, which yields (2), in which the structure velocity \mathbf{u}_2 and the Lagrange multiplier $\boldsymbol{\lambda}$ should be viewed as prescribed data. We describe two ways of discretizing this subproblem: the variational multiscale (VMS) approach³ (Sect. 3.1.1) and the divergence-conforming B-spline approach (Sect. 3.1.2).

3.1.1 Variational Multiscale Formulation

Issues of discrete stability and turbulence modeling are simultaneously addressed by the variational multiscale (VMS) [83] formulation of [58]. In short, it substitutes an ansatz for subgrid velocities and pressures into the weak fluid subproblem. This ansatz is consistent with the strong form of the Navier–Stokes equations, so that the formulation smoothly transitions to high-order-accurate direct numerical simulation as approximation spaces are refined.

The mesh-dependent VMS formulation is posed on a collection of disjoint fluid elements $\{\Omega^e\}$ such that $\overline{\Omega}_1 = \cup_e \overline{\Omega}^e$. $\{\Omega^e\}$, Ω_1 , and Γ remain time-dependent, but, when there is no risk of confusion, we drop the subscript t to simplify notation. The superscript h indicates association with discrete spaces defined over these elements. The mesh $\{\Omega^e\}$ deforms with velocity $\hat{\mathbf{u}}^h$. Let \mathcal{V}_u^h and \mathcal{V}_p^h be discrete velocity and pressure spaces defined over $\{\Omega^e\}$. The semi-discrete VMS fluid subproblem is: Find $\mathbf{u}_1^h \in \mathcal{V}_u^h$ and $p^h \in \mathcal{V}_p^h$ such that, for all $\mathbf{w}_1^h \in \mathcal{V}_u^h$ and $q^h \in \mathcal{V}_p^h$,

$$\begin{aligned} B_1^{\text{VMS}}(\{\mathbf{u}_1^h, p^h\}, \{\mathbf{w}_1^h, q^h\}; \hat{\mathbf{u}}^h) - F_1^{\text{VMS}}(\{\mathbf{w}_1^h, q^h\}) \\ + \int_{\Gamma} \mathbf{w}_1^h \cdot (\lambda \mathbf{n}_2) d\Gamma + \int_{\Gamma} \mathbf{w}_1^h \cdot \beta(\mathbf{u}_1^h - \mathbf{u}_2) d\Gamma = 0, \end{aligned} \quad (9)$$

where

$$\begin{aligned} B_1^{\text{VMS}}(\{\mathbf{u}, p\}, \{\mathbf{w}, q\}; \hat{\mathbf{u}}) &= \int_{\Omega_1} \mathbf{w} \cdot \rho_1 \left(\frac{\partial \mathbf{u}}{\partial t} \Big|_{\hat{\mathbf{x}}} + (\mathbf{u} - \hat{\mathbf{u}}) \cdot \nabla \mathbf{u} \right) d\Omega \\ &+ \int_{\Omega_1} \boldsymbol{\varepsilon}(\mathbf{w}) : \boldsymbol{\sigma}_1 d\Omega + \int_{\Omega_1} q \nabla \cdot \mathbf{u} d\Omega \\ &- \gamma \int_{\Gamma_{1h}} \mathbf{w} \cdot \rho_1 \{(\mathbf{u} - \hat{\mathbf{u}}) \cdot \mathbf{n}_1\}_- \mathbf{u} d\Gamma \end{aligned}$$

³We use of the term ‘‘VMS’’ in this chapter to refer to the specific VMS formulation explained in Sect. 3.1.1, applied to equal-order pressure–velocity discretizations. Our choice of terminology should not be taken to mean that the concept of VMS analysis is incompatible with div-conforming B-splines, which is demonstrably [82] not true.

$$\begin{aligned}
 & - \sum_e \int_{\Omega^e} \left((\mathbf{u} - \hat{\mathbf{u}}) \cdot \nabla \mathbf{w} + \frac{1}{\rho_1} \nabla q \right) \cdot \mathbf{u}' \, d\Omega \\
 & - \sum_e \int_{\Omega^e} p' \nabla \cdot \mathbf{w} \, d\Omega \\
 & + \sum_e \int_{\Omega^e} \mathbf{w} \cdot (\mathbf{u}' \cdot \nabla \mathbf{u}) \, d\Omega \\
 & - \sum_e \int_{\Omega^e} \frac{1}{\rho_1} \nabla \mathbf{w} : (\mathbf{u}' \otimes \mathbf{u}') \, d\Omega \\
 & + \sum_e \int_{\Omega^e} (\mathbf{u}' \cdot \nabla \mathbf{w}) \bar{\tau} \cdot (\mathbf{u}' \cdot \nabla \mathbf{u}) \, d\Omega, \quad (10)
 \end{aligned}$$

and

$$F_1^{\text{VMS}}(\{\mathbf{w}, q\}) = F_1(\{\mathbf{w}, q\}). \quad (11)$$

The forms B_1^{VMS} and F_1^{VMS} are semi-discrete counterparts of B_1 and F_1 . \mathbf{u}' is the fine scale velocity ansatz,

$$\mathbf{u}' = -\tau_M \left(\rho_1 \left(\frac{\partial \mathbf{u}}{\partial t} \Big|_{\hat{\mathbf{x}}} + (\mathbf{u} - \hat{\mathbf{u}}) \cdot \nabla \mathbf{u} - \mathbf{f} \right) - \nabla \cdot \boldsymbol{\sigma}_1 \right), \quad (12)$$

and p' is the fine scale pressure,

$$p' = -\rho_1 \tau_C \nabla \cdot \mathbf{u}. \quad (13)$$

The stabilization parameters τ_M , τ_C , and $\bar{\tau}$ are defined as

$$\tau_M = \left(s \left(\frac{4}{\Delta t^2} + (\mathbf{u} - \hat{\mathbf{u}}) \cdot \mathbf{G}(\mathbf{u} - \hat{\mathbf{u}}) + C_I \left(\frac{\mu}{\rho_1} \right)^2 \mathbf{G} : \mathbf{G} \right) \right)^{-1/2}, \quad (14)$$

$$\tau_C = (\tau_M \text{tr} \mathbf{G})^{-1}, \quad (15)$$

$$\bar{\tau} = (\mathbf{u}' \cdot \mathbf{G} \mathbf{u}')^{-1/2}, \quad (16)$$

where Δt is a timescale associated with the (currently unspecified) temporal discretization, C_I is a dimensionless positive constant derived from element-wise inverse estimates [84, 85], and \mathbf{G} generalizes element size to physical elements mapped through $\mathbf{x}(\boldsymbol{\xi})$ from a parametric parent element: $G_{ij} = \xi_{k,i} \xi_{k,j}$. s is a dimensionless field such that, in most of Ω_1 , $s = 1$, but, in an $\mathcal{O}(h)$ neighborhood of Γ , $s = s^{\text{shell}} \geq 1$. We introduced this field in [77] to improve mass conservation near immersed boundaries. A theoretical motivation for this scaling is given in [86], and a numerical investigation of its effect is given in [77].

3.1.2 Divergence Conforming B-splines

A way to totally eliminate mass loss and obtain pointwise divergence-free velocity solutions is to discretize the fluid in a divergence-conforming (or div-conforming) manner, such that the divergence of every vector-valued function in the discrete velocity space is a member of the discrete pressure space. If this property is satisfied, then weak mass conservation implies strong (pointwise) mass conservation. A discretization of this type was developed for Stokes and Navier–Stokes flows by Evans and Hughes [59, 60, 87]. Evans and Hughes used B-splines to construct velocity and pressure spaces with the necessary properties, then directly posed the weak problem $B_1(\{\mathbf{u}_1^h, p^h\}, \{\mathbf{w}_1^h, q^h\}; \mathbf{0}) = F_1(\{\mathbf{w}_1^h, q^h\})$ over these discrete spaces. A caveat to the above reasoning is that, to truly obtain velocities that conform to the incompressibility constraint, one would need to solve the discrete algebraic problem *exactly*, which is impractical for realistic problems. We demonstrate in the 3D numerical examples of Sects. 6.2 and 6.3, however, that the benefits of divergence-conforming discretizations persist through common approximations in the assembly and solution of the algebraic problem.

Evans and Hughes used Nitsche’s method to enforce no-slip boundary conditions. For the computations of this chapter, the regularity of the fluid velocity solution is at most $H^{3/2-\epsilon}(\Omega_1)$ and we use, for simplicity, a weakly consistent penalty method, altering the problem to be

$$B_1(\{\mathbf{u}_1, p\}, \{\mathbf{w}_1, q\}; \mathbf{0}) + C_{\text{pen}} \int_{\Gamma_{\text{pen}}} (\mathbf{u}_1 - \mathbf{g}) \cdot \mathbf{w}_1 \, d\Gamma = F_1(\{\mathbf{w}_1, q\}) , \quad (17)$$

where $C_{\text{pen}} > 0$ is a penalty parameter and \mathbf{g} is the desired velocity on $\Gamma_{\text{pen}} \subset \partial\Omega_1$.

Construction for Rectangular Domains

Suppose, for now, that Ω_1 is an axis-aligned d -dimensional rectangle. Then physical space can serve directly as a d -variate B-spline parameter space.⁴ Define a d -variate scalar B-spline space for the pressure on Ω_1 . Then, for $1 \leq i \leq d$, we can k -refine the pressure space once in the i th parametric direction to obtain a scalar space for the i th Cartesian velocity component. Due to well-known properties of B-splines under differentiation [88], the i th partial derivative of the i th velocity component will then be in the pressure space. The scalar basis functions of the velocity component spaces can be multiplied by their respective unit vectors to obtain a vector-valued basis for the discrete velocity space. The divergence of a velocity will therefore be a sum of d scalar functions in the pressure space.

⁴For readers unfamiliar with the construction and basic properties of B-splines, a comprehensive explanation can be found in [88].

Precise definitions are given in [59, Section 5.2]. In the notation of the cited reference, the velocity space is $\widehat{\mathcal{RT}}_h$ and the pressure space is $\widehat{\mathcal{W}}_h$. Following the terminology of [59], if the pressure space has polynomial degree k' in all directions, the entire pressure–velocity discretization is said to be of degree k' , despite the presence of $(k' + 1)$ -degree polynomials in the velocity component spaces.

Generalization to Non-rectangular Domains

Div-conforming B-splines are not limited to rectangular domains. A point \mathbf{X} in a rectangular parametric domain $\widehat{\Omega}$ may be mapped to a point \mathbf{x} in a non-rectangular physical domain Ω by $\mathbf{x} = \boldsymbol{\phi}(\mathbf{X})$. Vector-valued velocity basis functions defined on $\widehat{\Omega}$ are then pushed forward using the Piola transform. For arbitrary parametric-space velocity function $\widehat{\mathbf{u}}$, its pushforward \mathbf{u} is

$$\mathbf{u}(\mathbf{x}) = \frac{1}{J(\mathbf{X})} \mathbf{F}(\mathbf{X}) \widehat{\mathbf{u}}(\mathbf{X}), \tag{18}$$

where

$$\mathbf{F} = \frac{\partial \boldsymbol{\phi}}{\partial \mathbf{X}} \iff F_{iJ} = \frac{\partial \phi_i}{\partial X_J} = \phi_{i,J}, \tag{19}$$

and $J = \det \mathbf{F}$. Using Nanson’s formula [81, (2.54)] and integration by parts, we get the Piola identity

$$\operatorname{div} \mathbf{u} = \frac{1}{J} \operatorname{DIV} \widehat{\mathbf{u}}, \tag{20}$$

where

$$\operatorname{div} \mathbf{u} = \frac{\partial u_j}{\partial x_j} = u_{j,j} \quad \text{and} \quad \operatorname{DIV} \widehat{\mathbf{u}} = \frac{\partial \widehat{u}_B}{\partial X_B} = \widehat{u}_{B,B}. \tag{21}$$

We would like the divergence of every pushed-forward velocity function to exist in the pushed-forward pressure space. For every $\widehat{\mathbf{u}}$ in the parametric velocity space, there exists \widehat{q} in the parametric pressure space such that $\widehat{q} = \operatorname{DIV} \widehat{\mathbf{u}}$. Then, recalling (20), the parametric pressure space function should be pushed forward by

$$q(\mathbf{x}) = \frac{1}{J(\mathbf{X})} \widehat{q}(\mathbf{X}). \tag{22}$$

Div-conforming B-splines may be used on even wider classes of geometries by joining deformed rectangular patches together with a discontinuous Galerkin approach [59, Section 6.5].

Stabilizing Advection

The Galerkin discretization used by Evans and Hughes can be straightforwardly augmented to include SUPG stabilization [89]. However, the pressure gradient in the momentum equation residual removes the property of the Galerkin approximation that the error in the velocity solution is independent of pressure interpolation error [60, (6.32)]. This property is valuable in the presence of immersed boundaries that induce large discontinuities in the exact pressure solution. In this work, we stabilize div-conforming discretizations with $\mathcal{O}(h)$ streamline diffusion: we add

$$+ \sum_e (\tau \rho_1 \mathbf{u}_1^h \cdot \nabla \mathbf{u}_1^h, \mathbf{u}_1^h \cdot \nabla \mathbf{w}_1^h)_{L^2(\Omega^e)} \quad (23)$$

to $B_1(\{\mathbf{w}_1^h, q^h\}, \{\mathbf{u}_1^h, p^h\})$, where $\{\Omega^e\}_{e=1}^{N_{\text{el}}}$ are the N_{el} Bézier elements of the B-spline mesh and

$$\tau = \begin{cases} (\mathbf{u}_1^h \cdot \mathbf{G}\mathbf{u}_1^h)^{-1/2} \mathbf{u}_1^h \cdot \mathbf{G}\mathbf{u}_1^h > 0 \\ 0 & \text{otherwise} \end{cases} \quad (24)$$

While this is only weakly consistent, we do not expect high convergence rates from immersed boundary discretizations of the type considered here, due to low regularity of the exact solution.

3.2 Structure Subproblem

Setting $\mathbf{w}_1 = \delta\lambda = \mathbf{0}$ isolates the structure subproblem (3), in which \mathbf{u}_2 and λ are considered prescribed data. This problem can be stably discretized using a Bubnov–Galerkin method. However, for $B_2(\mathbf{y}, \mathbf{w})$ to remain bounded, \mathbf{y} and \mathbf{w} need to be in $H^2(\Gamma)$. It is sufficient for discrete spaces to be in $C^1(\Gamma)$. Traditional finite element spaces do not satisfy this requirement. However, isogeometric spline spaces can be made C^1 if geometry allows. Typical BHV leaflet geometries can be accurately modeled by C^1 spline surfaces, so, for the purposes of this chapter, the semidiscrete structure subproblem amounts to choosing \mathcal{V}_y in (3) to be (and enrichment of) the smooth spline space used to model the geometry. The implementation of such discretizations is documented exhaustively in [64]. We augment this discretization with penalty-based contact, as described in [77], as mentioned in Remark 1.

4 Dynamic Augmented Lagrangian Coupling

The augmented Lagrangian coupling the subproblems is discretized using a semi-implicit time integration scheme, in which the penalty is treated implicitly and the Lagrange multiplier is updated explicitly. We call this the *dynamic augmented*

Lagrangian (DAL) method. DAL circumvents difficulties with fully implicit coupling, while forbidding leakage through the structure in steady-state solutions and retaining the stability that eludes fully explicit approaches.

4.1 Separation of Normal and Tangential Coupling

The constraint that $\mathbf{u}_1 = \mathbf{u}_2$ on Γ can be separated into no-penetration

$$\mathbf{u}_1 \cdot \mathbf{n}_2 = \mathbf{u}_2 \cdot \mathbf{n}_2 \tag{25}$$

and no-slip

$$\mathbf{u}_1 - (\mathbf{u}_1 \cdot \mathbf{n}_2) \mathbf{n}_2 = \mathbf{u}_2 - (\mathbf{u}_2 \cdot \mathbf{n}_2) \mathbf{n}_2, \tag{26}$$

where \mathbf{n}_2 is normal to Γ . These constraints are enforced by normal and tangential components of λ .

No-penetration is critical to the qualitative structure of solutions. No-slip is less essential, and strong enforcement may even be detrimental to solution quality on coarse meshes [90–94]. We therefore discretize these constraints differently. For no-penetration, we discretize a scalar multiplier field, $\lambda = \lambda \cdot \mathbf{n}_2$. For no-slip, we approximate the tangential component of λ by a weakly consistent penalty force. Because Γ_t can cut through the fluid domain in arbitrary ways, we do not attempt to construct inf-sup stable combinations of velocity and multiplier spaces. Instead, we circumvent the inf-sup condition by regularizing the no-penetration constraint residual:

$$(\mathbf{u}_1 - \mathbf{u}_2) \cdot \mathbf{n}_2 \rightarrow (\mathbf{u}_1 - \mathbf{u}_2) \cdot \mathbf{n}_2 - \frac{r}{\beta} \lambda, \tag{27}$$

where $r \geq 0$ is a dimensionless constant. Much as the slip penalization can be derived as a degenerate case of Nitsche’s method [77, Section 4.1], the regularization of the no-penetration constraint can be viewed as a degenerate case of strongly consistent Barbosa–Hughes stabilization [95].

The problem we discretize in time is then: Find $\mathbf{u}_1 \in \mathcal{S}_u$, $p \in \mathcal{S}_p$, $\mathbf{y} \in \mathcal{S}_d$, and $\lambda \in \mathcal{S}_\ell$ such that, for all test functions $\mathbf{w}_1 \in \mathcal{V}_u$, $q \in \mathcal{V}_p$, $\mathbf{w}_2 \in \mathcal{V}_d$, and $\delta\lambda \in \mathcal{V}_\ell$

$$\begin{aligned} & B_1(\{\mathbf{w}_1, q\}, \{\mathbf{u}_1, p\}; \hat{\mathbf{u}}) - F_1(\{\mathbf{w}_1, q\}) + B_2(\mathbf{w}_2, \mathbf{y}) - F_2(\mathbf{w}_2) \\ & + \int_{\Gamma_t} (\mathbf{w}_1 - \mathbf{w}_2) \cdot \lambda \mathbf{n}_2 \, d\Gamma \\ & + \int_{\Gamma_t} (\mathbf{w}_1 - \mathbf{w}_2) \cdot \tau_{\text{NOR}}^B ((\mathbf{u}_1 - \mathbf{u}_2) \cdot \mathbf{n}_2) \mathbf{n}_2 \, d\Gamma \end{aligned}$$

$$\begin{aligned}
& + \int_{\Gamma_t} (\mathbf{w}_1 - \mathbf{w}_2) \cdot \boldsymbol{\tau}_{\text{TAN}}^B ((\mathbf{u}_1 - \mathbf{u}_2) - ((\mathbf{u}_1 - \mathbf{u}_2) \cdot \mathbf{n}_2) \mathbf{n}_2) \, d\Gamma \\
& + \int_{\Gamma_t} \delta\lambda \cdot \left((\mathbf{u}_1 - \mathbf{u}_2) \cdot \mathbf{n}_2 - \frac{r\lambda}{\tau_{\text{NOR}}^B} \right) \, d\Gamma = 0, \tag{28}
\end{aligned}$$

where we split the penalty term into normal and tangential components. We propose to scale the tangential penalty like

$$\tau_{\text{TAN}}^B = C_{\text{TAN}} \frac{\mu}{h}, \tag{29}$$

where C_{TAN} is a dimensionless $\mathcal{O}(1)$ constant and h is a measure of the fluid element diameter, with units of length. We propose that the normal penalty scale like

$$\tau_{\text{NOR}}^B = \max \left\{ C_{\text{NOR}}^{\text{inert}} \frac{\rho_1 h}{\Delta t}, C_{\text{NOR}}^{\text{visc}} \frac{\mu}{h} \right\}, \tag{30}$$

where $C_{\text{NOR}}^{\text{inert}}$ and $C_{\text{NOR}}^{\text{visc}}$ are dimensionless constants and Δt is a time scale from the temporal discretization.

4.2 Time Integration Algorithm

We now state the time-marching procedure for the coupled system. The algorithm computes approximate solutions discrete time levels, indexed by n and separated by steps of size Δt . At time level n , the discrete fluid velocity is defined by a coefficient vector \mathbf{U}^n , the fluid time derivative by $\dot{\mathbf{U}}^n$, the fluid pressure by \mathbf{P}^n , and the structure displacement, velocity, and acceleration by \mathbf{Y}^n , $\dot{\mathbf{Y}}^n$, and $\ddot{\mathbf{Y}}^n$. The multiplier at level n is λ^n , considered a function with domain Γ_t , and represented discretely as a set of samples at quadrature points of a (Lagrangian) integration rule on Γ_t . Consider solution variables at level n known. The first step of DAL is to construct a system of equations for all $(n+1)$ -level fluid and structure unknowns, with λ^{n+1} kept equal to λ^n :

$$\text{Res} \left(\mathbf{U}^{n+\alpha_f}, \dot{\mathbf{U}}^{n+\alpha_m}, \mathbf{Y}^{n+\alpha_f}, \dot{\mathbf{Y}}^{n+\alpha_f}, \ddot{\mathbf{Y}}^{n+\alpha_m}, \mathbf{P}^{n+1}, \lambda^{n+1} (= \lambda^n) \right) = \mathbf{0}, \tag{31}$$

$$\mathbf{U}^{n+1} = \mathbf{U}^n + \Delta t \left((1 - \gamma) \dot{\mathbf{U}}^n + \gamma \dot{\mathbf{U}}^{n+1} \right), \tag{32}$$

$$\dot{\mathbf{U}}^{n+\alpha_m} = \dot{\mathbf{U}}^n + \alpha_m \left(\dot{\mathbf{U}}^{n+1} - \dot{\mathbf{U}}^n \right), \tag{33}$$

$$\mathbf{U}^{n+\alpha_f} = \mathbf{U}^n + \alpha_f \left(\mathbf{U}^{n+1} - \mathbf{U}^n \right), \tag{34}$$

$$\mathbf{Y}^{n+1} = \mathbf{Y}^n + \Delta t \dot{\mathbf{Y}}^n + \frac{\Delta t^2}{2} \left((1 - 2\beta) \ddot{\mathbf{Y}}^n + 2\beta \ddot{\mathbf{Y}}^{n+1} \right), \tag{35}$$

$$\dot{\mathbf{Y}}^{n+1} = \dot{\mathbf{Y}}^n + \Delta t \left((1 - \gamma) \ddot{\mathbf{Y}}^n + \gamma \ddot{\mathbf{Y}}^{n+1} \right), \quad (36)$$

$$\ddot{\mathbf{Y}}^{n+\alpha_m} = \ddot{\mathbf{Y}}^n + \alpha_m \left(\ddot{\mathbf{Y}}^{n+1} - \ddot{\mathbf{Y}}^n \right), \quad (37)$$

$$\dot{\mathbf{Y}}^{n+\alpha_f} = \dot{\mathbf{Y}}^n + \alpha_f \left(\dot{\mathbf{Y}}^{n+1} - \dot{\mathbf{Y}}^n \right), \quad (38)$$

$$\mathbf{Y}^{n+\alpha_f} = \mathbf{Y}^n + \alpha_f \left(\mathbf{Y}^{n+1} - \mathbf{Y}^n \right), \quad (39)$$

where α_m , α_f , β , and γ are time integration parameters. $\text{Res}(\dots)$ is the algebraic residual corresponding to the discretization of (28) with $\delta\lambda = 0$. This penalty-coupled problem is resolved by block iteration, which alternates between solving for fluid and structure increments, as described further in Sect. 4.3. Equations (31)–(39) are based on the generalized- α method [96]. Following [97, Section 4.4], we work within a subset of generalized- α methods, parameterized by $\rho_\infty \in [0, 1]$, which controls numerical damping and defines the free parameters as

$$\alpha_m = \frac{1}{2} \left(\frac{3 - \rho_\infty}{1 + \rho_\infty} \right), \quad \alpha_f = \frac{1}{1 + \rho_\infty}, \quad (40)$$

$$\gamma = \frac{1}{2} + \alpha_m - \alpha_f, \quad \beta = \frac{1}{4} \left(1 + \alpha_m - \alpha_f \right)^2. \quad (41)$$

The backward Euler method can also be conveniently implemented within the generalized- α predictor–multi-corrector scheme of [97] by setting the generalized- α parameters to $\alpha_m = \alpha_f = \gamma = \beta = 1$ and modifying the displacement predictor.

Note that, because the multiplier is fixed in (31)–(39), the (regularized) α -level constraint residual

$$\mathbf{R}^{n+\alpha} = \left(\left(\mathbf{u}_1^h \right)^{n+\alpha_f} - \left(\mathbf{u}_2^h \right)^{n+\alpha_f} \right) \cdot \mathbf{n}_2^{n+\alpha_f} - \frac{r\lambda^{n+1}}{\tau_{\text{NOR}}^B} \quad (42)$$

is not necessarily zero on $\Gamma_{t+\alpha_f}$. To motivate the development of the multiplier update step in DAL, consider the case of $r = 0$. If $\mathbf{R}^{n+\alpha} = 0$ and $r = 0$, then the normal component of the α -level penalty force, $\tau_{\text{NOR}}^B \mathbf{R}^{n+\alpha}$, will be zero and the normal α -level fluid–structure force will be due only to the Lagrange multiplier, λ^{n+1} . This suggests the explicit update

$$\lambda^{n+1} \leftarrow \lambda^{n+1} + \tau_{\text{NOR}}^B \mathbf{R}^{n+\alpha}, \quad (43)$$

in which λ^{n+1} is set equal to the α -level fluid–structure forcing. Equations (31)–(39) are of course no longer satisfied with the updated λ^{n+1} , but one may attempt to iterate the steps

1. Solve (31)–(39) with λ^{n+1} fixed.
2. Update λ^{n+1} by (43).

until $\|R^{n+\alpha}\|_{L^2(\Gamma_f)}$ is converged to some tolerance. As explained in [77, Section 4.2.1], the $r = 0$ case of this iteration corresponds to the classic augmented Lagrangian algorithm of [98, 99]. For $r = 0$, though, the convergence criterion of $\|R^{n+\alpha}\|_{L^2(\Gamma_f)} < \epsilon$ is too strict to arrive at a non-locking solution; it effectively demands pointwise constraint satisfaction between non-matching velocity spaces of the fluid and structure. We found, accordingly, that the iteration does not typically converge, but circumvented this difficulty by truncating to a single pass, leading to the semi-implicit time marching scheme of first solving (31)–(39) with $\lambda^{n+1} = \lambda^n$, then updating λ^{n+1} by (44) and continuing directly to the next time step, i.e.,

$$\lambda^{n+1} = \lambda^n + \tau_{\text{NOR}}^B R^{n+\alpha}. \quad (44)$$

This augmented-Lagrangian-based explicit multiplier update is the distinguishing feature of DAL. Use of $r = 0$ is effective for transient problems, but may run into difficulties in the steady limit, when the Lagrange multiplier and velocity discrete spaces are not chosen stably. Choosing $r > 0$ can improve robustness. In that case, (44) is an implicit formula, but it can be recast in explicit form:

$$\lambda^{n+1} = \frac{\lambda^n + \tau_{\text{NOR}}^B \left((\mathbf{u}_1^h)^{n+\alpha_f} - (\mathbf{u}_2^h)^{n+\alpha_f} \right) \cdot \mathbf{n}_2^{n+\alpha_f}}{1 + r}. \quad (45)$$

Some caution is warranted, however, in perturbing the kinematic constraint. Section 4.4.4 provides an illustrative example of the effects of this consistency error.

4.3 Block Iterative Solution of the Implicit Problem

The implicit step of DAL amounts to a penalty regularization of fluid–structure coupling, with a prescribed loading $\lambda^n \mathbf{n}^{n+\alpha_f}$ along $\Gamma^{n+\alpha_f}$. The penalty value can be moderate, rendering the regularized problem much easier to solve. A simple block-iterative procedure turns out to be practical, even for applications with light structures and heavy, incompressible fluids.

Consider $R_f(u_f, u_s)$ to be the nonlinear residual for the fully discrete fluid subproblem at a particular time step, which depends on discrete fluid and structure solutions, u_f and u_s . Likewise, $R_s(u_f, u_s)$ is the residual for the discrete structure subproblem. The block-iterative procedure to find a root of (R_f, R_s) is to start with guesses for u_f and u_s and repeat

1. Assemble $R_f(u_f, u_s)$ and a(n approximate) tangent matrix, $A_f \approx \partial R_f / \partial u_f$.
2. Solve the linear system $A_f \Delta u_f = -R_f$ for the fluid solution increment.
3. Update the fluid solution: $u_f \leftarrow u_f + \Delta u_f$.
4. Assemble $R_s(u_f, u_s)$ and $A_s \approx \partial R_s / \partial u_s$.
5. Solve $A_s \Delta u_s = -R_s$ for the structure solution increment.
6. Update the structure solution: $u_s \leftarrow u_s + \Delta u_s$.

until R_f and R_s are sufficiently converged. To ensure predictable run-times and avoid stagnation in pathological configurations, we typically choose a fixed number of iterations rather than a convergence tolerance. While it is possible that error from isolated, poorly solved time steps can pollute the future of an unsteady solution, we find this *ad hoc* procedure effective for predicting quantities of engineering interest.

4.4 Discussion

We summarize here some alternate interpretations and qualitative analysis from [77, 100] of the algorithm stated in Sect. 4.2.

4.4.1 Modified Equation Interpretation of DAL

When $r = 0$, the multiplier becomes an accumulation of penalty tractions from previous time steps. This is equivalent to replacing the multiplier and normal penalty terms

$$\int_{\Gamma_t} (\mathbf{w}_1 - \mathbf{w}_2) \cdot (\lambda \mathbf{n}_2) d\Gamma + \int_{\Gamma_t} ((\mathbf{w}_1 - \mathbf{w}_2) \cdot \mathbf{n}_2) \tau_{\text{NOR}}^B ((\mathbf{u}_1 - \mathbf{u}_2) \cdot \mathbf{n}_2) d\Gamma \quad (46)$$

by a penalization of (a backward Euler approximation of) the time integral of pointwise normal velocity differences on the immersed surface Γ_t

$$\int_{\Gamma_t} \left\{ \frac{\tau_{\text{NOR}}^B}{\Delta t} (\mathbf{w}_1(\mathbf{x}, t) - \mathbf{w}_2(\mathbf{x}, t)) \cdot \mathbf{n}_2(\mathbf{x}, t) \int_0^t \left(\mathbf{u}_1(\boldsymbol{\varphi}_\tau(\boldsymbol{\varphi}_t^{-1}(\mathbf{x})), \tau) - \mathbf{u}_2(\boldsymbol{\varphi}_\tau(\boldsymbol{\varphi}_t^{-1}(\mathbf{x})), \tau) \right) \cdot \mathbf{n}_2(\boldsymbol{\varphi}_\tau(\boldsymbol{\varphi}_t^{-1}(\mathbf{x})), \tau) d\tau \right\} d\Gamma, \quad (47)$$

where $\boldsymbol{\varphi}_\tau(\mathbf{X})$ gives the spatial position at time τ of material point $\mathbf{X} \in \Gamma_0$ and $d\Gamma$ indicates integration over $\mathbf{x} \in \Gamma_t$. To see this, first define (at fixed \mathbf{X})

$$\lambda^{\text{reg}}(t) = \frac{\tau_{\text{NOR}}^B}{\Delta t} \int_0^t (\mathbf{u}_1(\tau) - \mathbf{u}_2(\tau)) \cdot \mathbf{n}_2(\tau) d\tau. \quad (48)$$

Then

$$(\dot{\lambda}^{\text{reg}}) = \frac{\partial \lambda^{\text{reg}}}{\partial t} \Big|_{\mathbf{X}} = \frac{\tau_{\text{NOR}}^B}{\Delta t} (\mathbf{u}_1 - \mathbf{u}_2) \cdot \mathbf{n}_2. \quad (49)$$

The normal forcing on Γ in the implicit step of the semi-implicit time integrator is

$$(\lambda^{\text{reg}})^{n+1} = (\lambda^{\text{reg}})^n + \Delta t (\lambda^{\text{reg}})^{n+1} \quad (50)$$

where $(\lambda^{\text{reg}})^n$ is a sum of all previous approximations of λ and $\Delta t (\lambda^{\text{reg}})^{n+1}$ is the current time step's penalty forcing. Thus the forcing (47) is accounted for in a fully implicit manner, using the stable backward Euler method.

For $r > 0$, we can draw a similar analogy, in which λ^{reg} advances through time by backward Euler integration of

$$\frac{1}{(1+r)} \left. \frac{\partial \lambda^{\text{reg}}}{\partial t} \right|_{\mathbf{x}} = \frac{\tau_{\text{NOR}}^B}{\Delta t} (\mathbf{u}_1 - \mathbf{u}_2) \cdot \mathbf{n}_2 - \frac{r}{\Delta t(1+r)} \lambda^{\text{reg}}. \quad (51)$$

Intuitively, the additional term causes a decay of λ^{reg} in the absence of constraint violation, which highlights its stabilizing effect.

4.4.2 Analogy to Artificial Compressibility

The differential equation given in (49) closely resembles the method of artificial compressibility [101]. In that scheme, the approximated Lagrange multiplier p representing pressure in an incompressible flow evolves in an analogous way to λ^{reg} (in the case $r = 0$):

$$\partial_t p = -\frac{1}{\delta} \nabla \cdot \mathbf{u}_1, \quad (52)$$

where the constraint is $\nabla \cdot \mathbf{u}_1 = 0$ (instead of $(\mathbf{u}_1 - \mathbf{u}_2) \cdot \mathbf{n}_2 = 0$), $1/\delta$ is the penalty parameter. A physical interpretation of DAL for FSI, similar to Chorin's original formulation of (52) in terms of a fictitious density variable, is that, for $r = 0$, DAL penalizes displacement of the fluid through the structure. This interpretation makes clear how penalizing the time integral of velocity prevents the steady creep of flow through a barrier.

4.4.3 Relation to Feedback Boundary Conditions

The time-continuous interpretation of DAL with $r = 0$ may be interpreted as a special case of an existing framework for enforcing Dirichlet boundary conditions on the unsteady Navier–Stokes equation. Goldstein et al. [102] proposed to apply concentrated surface forcing of the form [102, (3)]

$$\mathbf{f}(\mathbf{x}_s, t) = \alpha \int_0^t \mathbf{u}_1(\mathbf{x}_s, \tau) d\tau + \beta \mathbf{u}_1(\mathbf{x}_s, t), \quad (53)$$

for all \mathbf{x}_s on a stationary solid boundary with parameters $\alpha \leq 0$ and $\beta \leq 0$. Goldstein et al. interpreted this method, which we refer to here as the feedback method, in the context of control theory, arguing heuristically that it provides negative feedback in the case of constraint violation.

The initial implementation of [102] used a spectral fluid discretization and applied smoothing to filter concentrated forces, reducing pollution effects from the global nature of the spectral basis functions (cf. [103, Chapter I, Section 2]). Goldstein and collaborators continue to use this methodology for DNS of turbulent flows [104–109]. Saiki and Biringen [110, 111] extended the concept of feedback forcing to finite difference fluid discretizations, using bilinear interpolation within grid cells to evaluate velocity at quadrature points of the immersed boundary and also to distribute concentrated feedback forces to grid points. Reference [110] was the first application of the approach to moving boundaries, in which (53) becomes (cf. [110, (1)] and (47))

$$\mathbf{f}(\boldsymbol{\varphi}_t(\mathbf{X}_s), t) = \alpha \int_0^t (\mathbf{u}_1(\boldsymbol{\varphi}_\tau(\mathbf{X}_s), \tau) - \mathbf{U}_2(\mathbf{X}_s, \tau)) d\tau + \beta (\mathbf{u}_1(\boldsymbol{\varphi}_\tau(\mathbf{X}_s), \tau) - \mathbf{U}_2(\mathbf{X}_s, \tau)) , \tag{54}$$

where $\boldsymbol{\varphi}_t(\mathbf{X}_s)$ represents the position at time t of a material point \mathbf{X}_s on the moving boundary with velocity $\mathbf{U}_2(\mathbf{X}_s, t)$. This naturally leads to FSI, and a recent series of papers [112–116] demonstrated that feedback forcing is robust and accurate for simulating light, flexible, immersed structures. A related approach has been used in the commercial code LS-DYNA [41] for decades, to study automobile airbag inflation and other challenging FSI problems [117–120], including heart valve simulation [42–45]. We have seen no documentation explicitly relating it to the feedback method, and assume that it was devised independently. The repeated rediscovery of this formulation by engineers studying difficult CFD and FSI problems suggests an inherent robustness to the approach.

4.4.4 Qualitative Effects of Multiplier Stabilization

The case of $r > 0$ is less physically intuitive than the $r = 0$ case. To provide some intuition for the influence of r , consider a model of plug flow through a blocked tube: a rigid barrier blocks a channel with slip boundaries, filled with a fluid assumed to have a velocity, $u\mathbf{e}_1$, that is constant across space, but may vary with time.

The ends of the channel are subject to pressures P_1 and P_2 , which define the pressure drop, $\Delta P = P_1 - P_2$. Suppose that the Lagrange multiplier field takes on a single constant value across the barrier. Then the steady solution of the semi-implicit time integration procedure described in Sect. 4.2 reduces to the conditions

1. Steadiness: $\lambda^{n+1} = \lambda^n = \lambda^\infty \Rightarrow \lambda^\infty = (\lambda^\infty + \tau_{\text{NOR}}^B u) / (1 + r)$.
2. Equilibrium: $\lambda^\infty + \tau_{\text{NOR}}^B u = \Delta P$.

Leakage is then given by $u = \frac{r \Delta P}{\tau_{\text{NOR}}^B (1+r)}$, which asymptotes to inverse scaling with the penalty parameter as $r \rightarrow \infty$ and to zero as $r \rightarrow 0$. For fixed $r > 0$, steady leakage converges to zero with refinement at the same rate as it would for a pure penalty method, but, if r is an adjustable parameter, one may reduce the steady-state leakage arbitrarily without impacting the solvability of the discrete problem at each time step.

5 Numerical Experiments

We demonstrate, through numerical experiments, that the DAL method is convergent. We summarize here results from [77, 86], considering both convergence of solutions in Sobolev norms for simple problems and convergence of quantities of interest in more complicated problems.

5.1 Navier–Stokes Flow with Immersed Boundaries

Consider, first, Navier–Stokes flow with Dirichlet conditions on immersed boundaries.

5.2 Taylor–Green Vortex

The Taylor–Green vortex is a solution to the 2D Navier–Stokes equations posed on the domain $\Omega = [-\pi, \pi]^2$ with periodic boundary conditions and no external forcing:

$$\mathbf{u}_{\text{TG}}(\mathbf{x}, t) = (\sin(x_1)\cos(x_2)\mathbf{e}_1 - \cos(x_1)\sin(x_2)\mathbf{e}_2) e^{-2\mu t/\rho}. \quad (55)$$

We construct an interesting test problem by prescribing $\mathbf{u} = \mathbf{u}_{\text{TG}}$ as an initial condition at $t = 0$ and also as a time-dependent Dirichlet boundary condition on a closed immersed boundary Γ , then adding a body force $\mathbf{f}_x = \mathbf{e}_1$. The body force induces a pressure gradient in the region enclosed by Γ without perturbing the velocity solution there. The velocity outside of the region enclosed by Γ is no longer equal to \mathbf{u}_{TG} for $t > 0$. There are jumps in the pressure and velocity derivatives along Γ , so the regularity of the velocity solution is representative of typical applications. We have not derived an exact solution on the entire domain, but one can easily measure error in a subset Ω^{err} of the region enclosed by Γ . In this section, we consider low Reynolds number flow, and choose $\mu = 0.01$. A high Reynolds-number test is carried out in Sect. 5.2.2.

Fig. 1 The non-rectilinear mesh of Ω avoids grid alignment with Γ

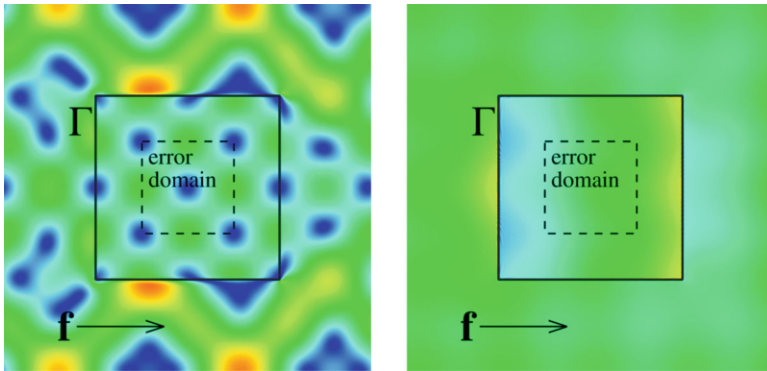
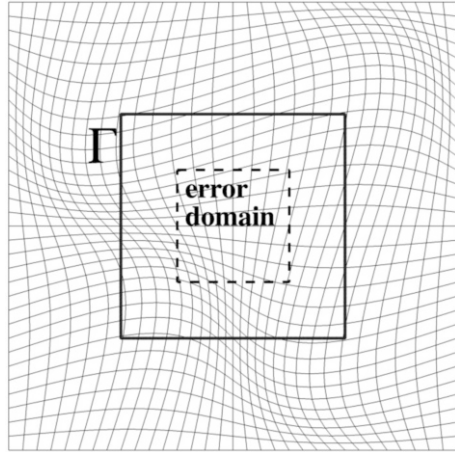


Fig. 2 Simultaneous velocity magnitude (left) and pressure (right) snapshots of the Navier–Stokes Taylor–Green problem, with annotations describing the problem setup

We choose $\Gamma = \partial((-\pi, \pi)^2)$. To avoid special behavior associated mesh-aligned immersed boundaries, we distort the background mesh, as shown in Fig. 1. Figure 2 illustrates the problem setup. Div-conforming B-splines of degree $k' = 1$ are used to discretize the velocity and pressure spaces, and backward Euler integration is applied in time. Error convergence is shown in Fig. 3, displaying nearly first-order rates.

5.2.1 Translating Taylor–Green Vortex

Adding a uniform velocity to an initial condition in a periodic domain yields a Galilean transformation of the original solution. In this section, we add $\mathbf{v} = -0.87\mathbf{e}_1 - 0.5\mathbf{e}_2$ to the initial condition of the Taylor–Green vortex and translate

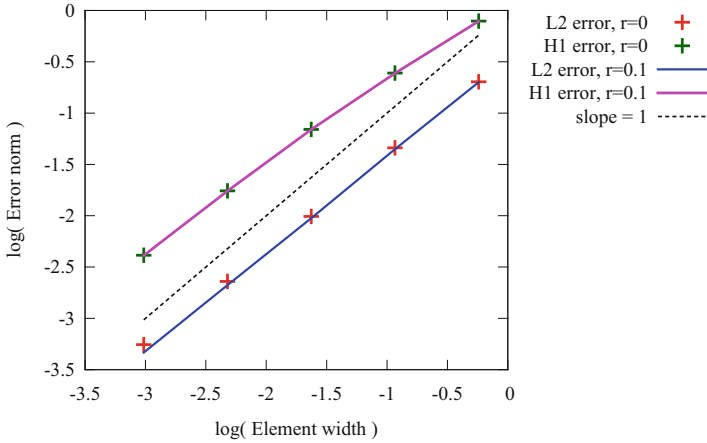
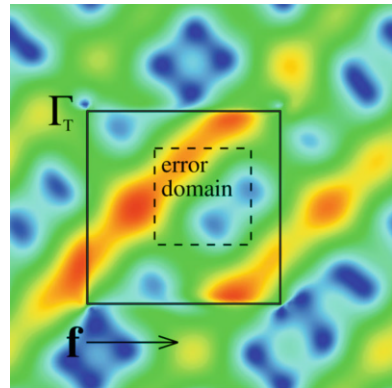


Fig. 3 Convergence of the $L^2(\Omega^{\text{err}})$ and $H^1(\Omega^{\text{err}})$ errors for $r = 0$ and $r = 0.1$ for Navier–Stokes flow with a stationary boundary and positive viscosity

Fig. 4 Annotated snapshot of velocity magnitude at time T for Navier–Stokes flow with moving boundaries and positive viscosity



Γ_i at the same velocity. The solution at time T is shown in Fig. 4. Figure 5 indicates that convergence on Ω^{err} remains intact.

5.2.2 Infinite Reynolds Number

To demonstrate the robustness at realistic Reynolds numbers, we repeat the test of Sect. 5.2.1 with $\mu = 0$. The exact solution becomes tangentially discontinuous at Γ_i . This behavior is captured reasonably well, as shown in Fig. 6. The nearly linear convergence rates in $L^2(\Omega^{\text{err}})$ and $H^1(\Omega^{\text{err}})$ are maintained, as shown in Fig. 7, despite the fact that the $H^1(\Omega)$ norm of the exact solution is not well-defined. This example uses $r = 0$, for reasons explained in [86].

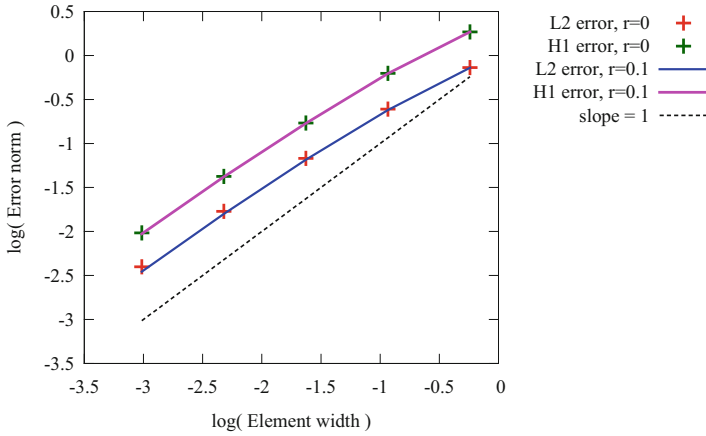
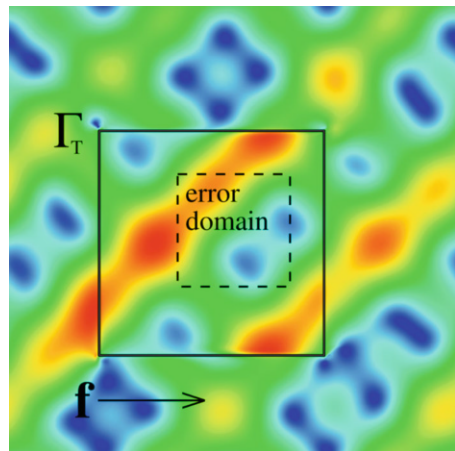


Fig. 5 Convergence of the $L^2(\Omega^{\text{err}})$ and $H^1(\Omega^{\text{err}})$ errors for $r = 0$ and $r = 0.1$ for Navier–Stokes flow with moving boundaries

Fig. 6 Annotated snapshot of velocity magnitude at time T for Navier–Stokes flow with moving boundaries and zero viscosity



5.3 2D Non-coapting Valve

This section considers a 2D valve-inspired benchmark problem investigated previously by Gil et al. [121], Hesch et al. [122], Wick [123], and Kadapa et al. [124]. The structure does not contact itself, so it is straightforward to compute converged solutions using verified body-fitted methods, making the problem a valuable benchmark for new immersed approaches.

5.3.1 Description of the Problem

The problem consists of two cantilevered elastic beams immersed in a 2D channel filled with incompressible Newtonian fluid, as shown in Fig. 8. The fluid and

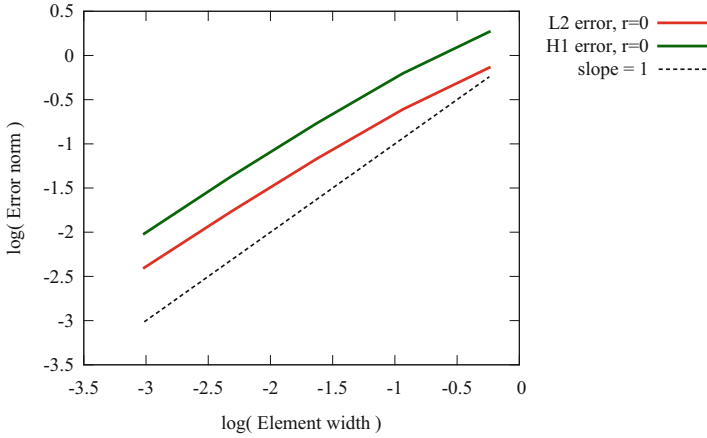


Fig. 7 Convergence of the $L^2(\Omega^{\text{err}})$ and $H^1(\Omega^{\text{err}})$ errors for $r = 0$ for Navier–Stokes flow with moving boundaries and zero viscosity

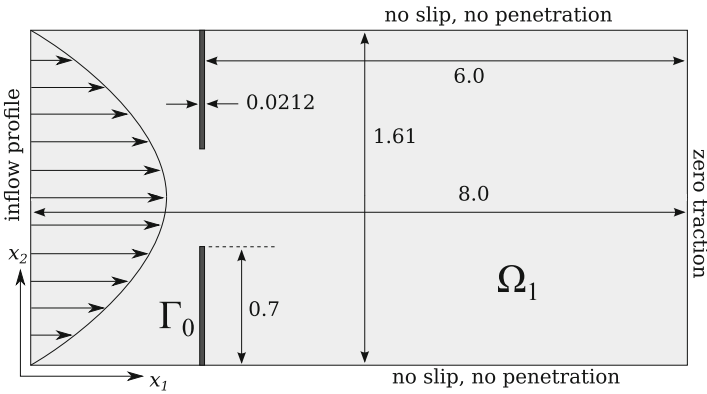


Fig. 8 Geometry and boundary conditions of the 2D heart valve benchmark

structure have equal densities of $\rho_1 = \rho_2 = 100$. The viscosity is $\mu = 10$. The structure is a St. Venant–Kirchhoff material with Young’s modulus $E = 5.6 \times 10^7$ and Poisson ratio $\nu = 0.4$. The top and bottom of the channel have no-slip boundary conditions, the right end is traction-free, and the left end has a prescribed, time-dependent velocity profile,

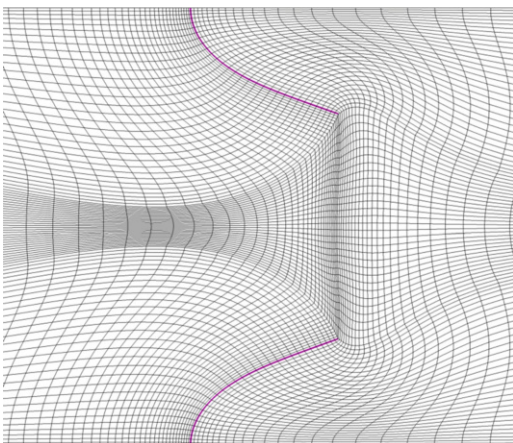
$$\mathbf{u}_1(y\mathbf{e}_2, t) = \begin{cases} 5(\sin(2\pi t) + 1.1)y(1.61 - y)\mathbf{e}_1, & t > 0 \\ \mathbf{0}, & \text{otherwise} \end{cases}, \quad (56)$$

where the origin of the spatial coordinate system is at the bottom left corner of the domain. The parameter γ in (5) is set to zero.



Fig. 9 The reference configuration of the body-fitted mesh for the 2D valve problem, with leaflets highlighted in magenta and areas of softened mesh highlighted in green

Fig. 10 The deformation of the body-fitted fluid mesh at $t = 0.5$



5.3.2 Body-Fitted Reference Computation

The mesh for the body-fitted reference computation is shown in Fig. 9. We use generalized- α time integration with $\rho_\infty = 0.5$ and a time step of $\Delta t = 0.005$. The selected resolution ensures that the displacement history of the upper beam tip changes negligibly with further refinement.

The fluid mesh deforms from one time step to the next according to the solution of a fictitious isotropic linear elastic problem that takes the location of the beam as a displacement boundary condition. The velocity of this deformation enters into (10) as $\hat{\mathbf{u}}^h$. Mesh quality is preserved throughout the deformation with Jacobian-based stiffening [97, 125–129]. In the present problem, we also find it necessary to soften the fictitious material governing the deformation of elements between the leaflets. The resulting deformed mesh at time $t = 0.5$ is shown in Fig. 10.

5.3.3 Immersogeometric Computations

We test three immersogeometric discretizations of the problem, using the VMS fluid formulation. The first, M1, evenly divides the fluid domain into 128×32 quadratic B-spline elements and each beam into 64 quadratic B-spline elements. The other

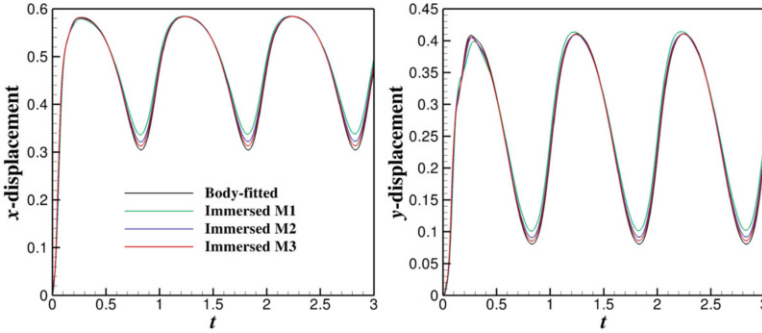


Fig. 11 The x - and y -displacements of the upper leaflet tip, computed on the immersed and body-fitted meshes

two are uniform refinements of M1. We refine also in time, using $\Delta t = 0.01$ with M1, $\Delta t = 0.005$ with M2, and $\Delta t = 0.0025$ with M3.

The time integration of the fluid–structure coupling is done using DAL with $r = 0$ and generalized- α parameters determined by $\rho_\infty = 0.5$. Following (29) and the low-Reynolds number branch of (30), we scale penalty parameters $\tau_{(\cdot)}^B$ inversely with mesh size, choosing $\tau_{(\cdot)}^B = 10^4$ on M1, $\tau_{(\cdot)}^B = 2 \times 10^4$ on M2, and $\tau_{(\cdot)}^B = 4 \times 10^4$ on M3. VMS parameters are scaled near the structure using $s^{\text{shell}} = 10^6$.

5.3.4 Comparison of Results

Figure 11 shows the x - and y -displacements of the upper beam tip for the body-fitted and immersed computations. Displacement histories from M1, M2, and M3 converge toward the body-fitted result. Comparisons of pressure contours at time $t = 0.5$ are given in Fig. 12, showing general agreement between immersogeometric and body-fitted flow fields. Velocity streamlines at $t = 0.5$ for M1 are shown in Fig. 13.

5.4 Benchmark Testing with Div-conforming B-splines

To verify the IMGA implementation using div-conforming B-splines for the fluid subproblem, we again use the 2D benchmark problem defined in Sect. 5.3. Although the problem domain is rectangular, we demonstrate convergence with distorted fluid meshes by deforming the interior of the parametric domain, as shown in Fig. 14. For the coarsest mesh, M1, the B-spline knot space is subdivided into 32×128 Bézier

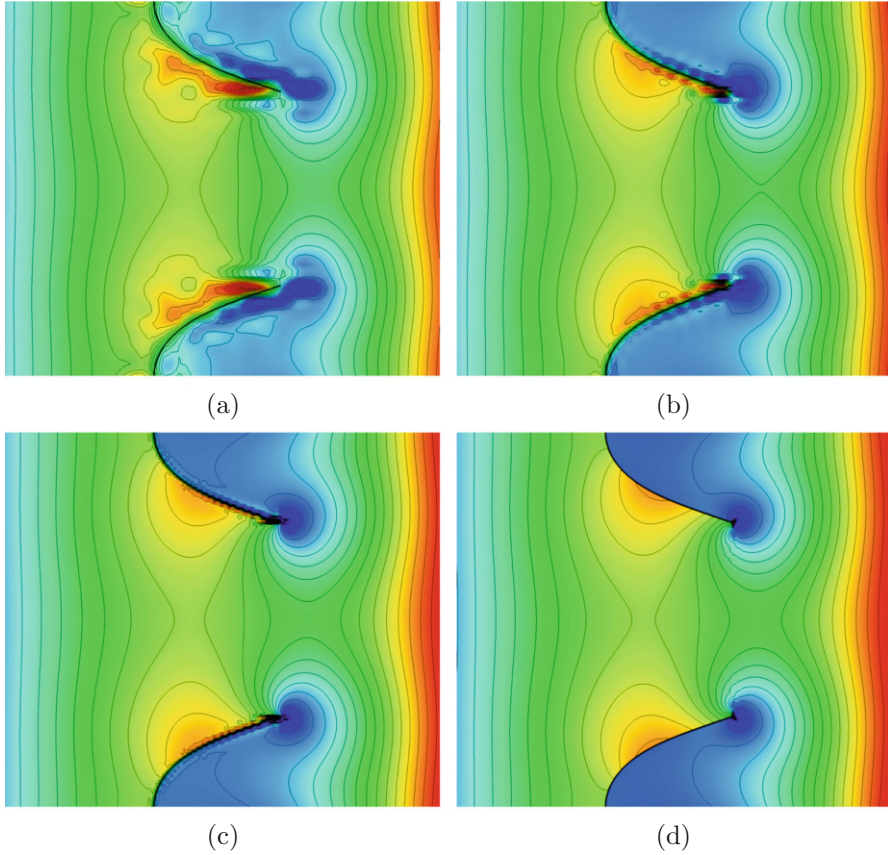


Fig. 12 Pressure contours at $t = 0.5$, from immersed boundary computations on M1, M2, and M3, along with the body-fitted reference. (a) Immersed M1. (b) Immersed M2. (c) Immersed M3. (d) Body-fitted reference

elements and div-conforming B-spline velocity and pressure spaces of degree $k' = 1$ are defined on this mesh. The meshes M2 and M3 are uniform refinements of M1.

Normal-direction Dirichlet boundary conditions on mesh boundaries are enforced strongly, while tangential boundary conditions are enforced by penalty. For computations on mesh $M(N + 1)$, penalty parameters are $\tau_{\text{NOR}}^B = \tau_{\text{TAN}}^B = C_{\text{no slip}} = 1000 \times 2^N$. We use the backward Euler method in time, with $\Delta t = 1.0 \times 10^{-2} \times 2^{-N}$.

Figures 15 and 16 compare x - and y -displacement histories of the upper beam tip in the three immersogeometric computations and the body-fitted reference. Figure 17 shows snapshots of the computed pressure and velocity solutions. Refinement of immersogeometric discretizations clearly brings this quantity of interest closer to the boundary-fitted reference curve.

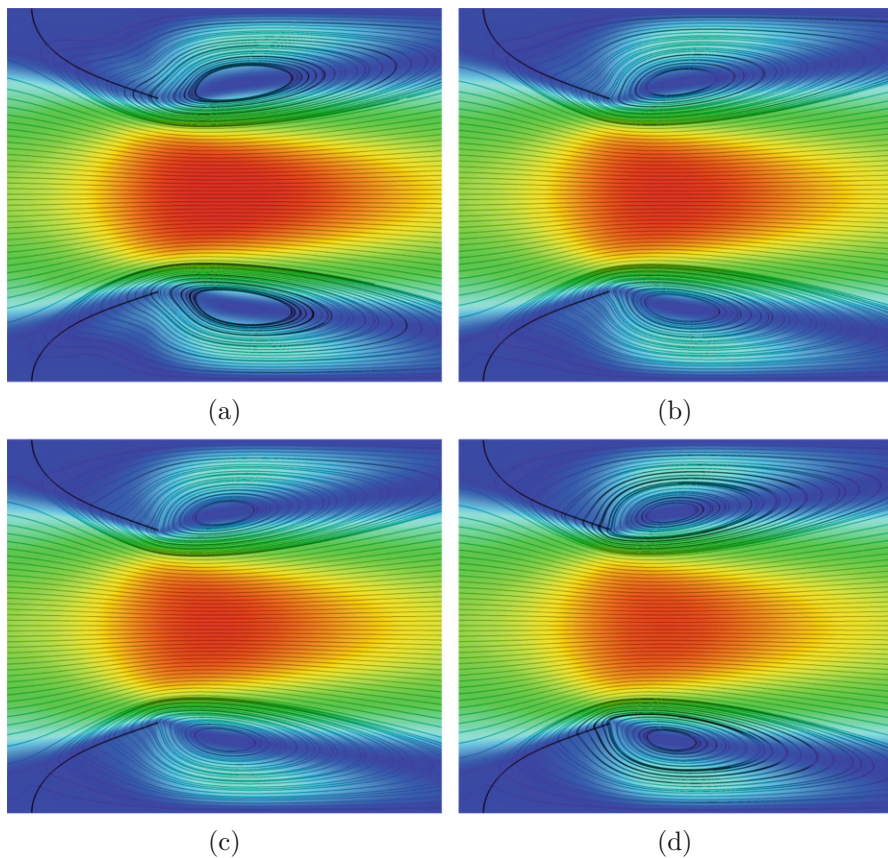


Fig. 13 Velocity streamlines superimposed on a velocity magnitude contour plot, at $t = 0.5$, from immersogeometric computations on M1, M2, and M3, and the body-fitted reference. **(a)** Immersed M1. **(b)** Immersed M2. **(c)** Immersed M3. **(d)** Body-fitted reference

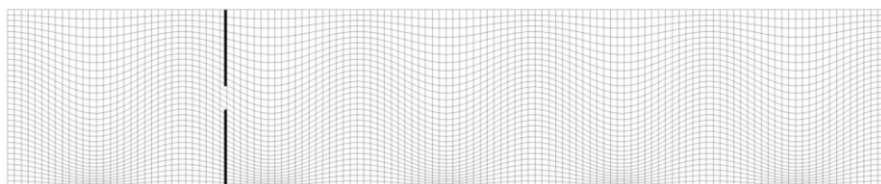


Fig. 14 The physical image of the B-spline parameter space, showing the mesh of unique knots (thin lines) for M1 in relation to the beams (thick lines)

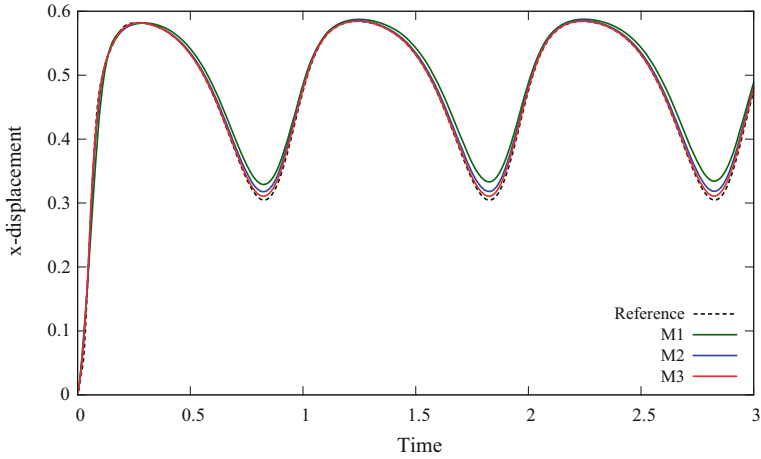


Fig. 15 The x-direction displacement of the tip of the upper beam

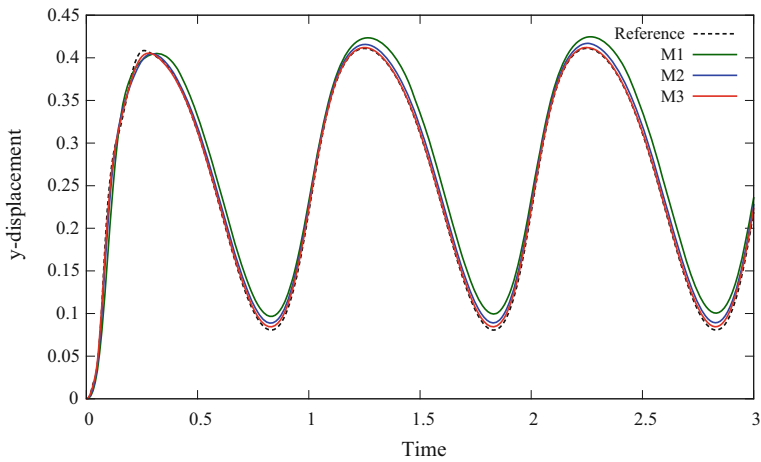


Fig. 16 The y-direction displacement of the tip of the upper beam

6 Application to BHV FSI Analysis

We first review some valve simulations using DAL-based IMGA. Section 6.3 then describes an initial effort toward validating the mathematical model for BHV FSI put forward in Sect. 2.

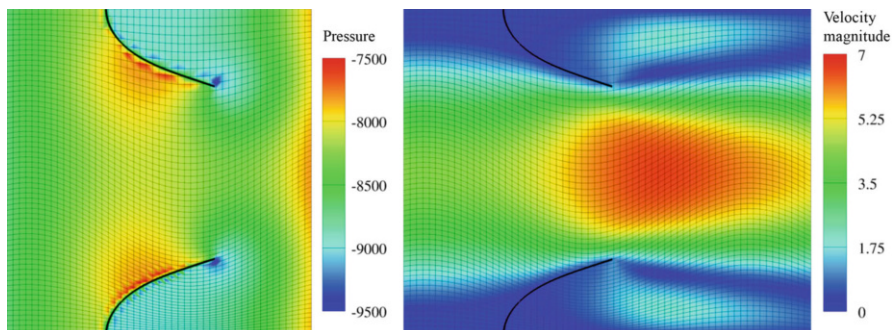


Fig. 17 The pressure field (left) and the velocity magnitude (right) at time $t = 0.5$ on M2

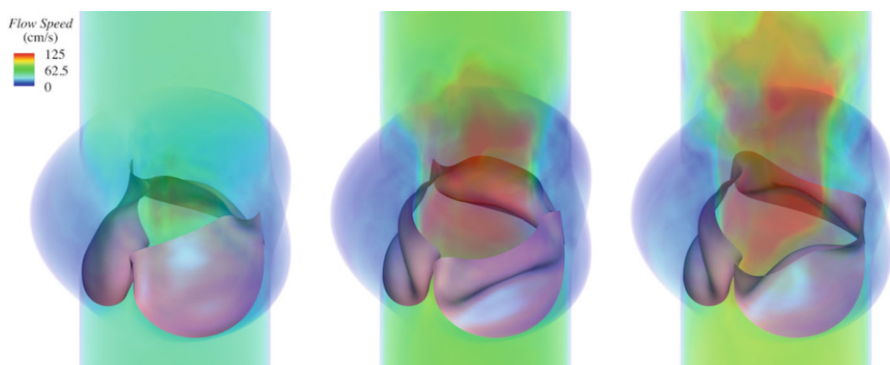


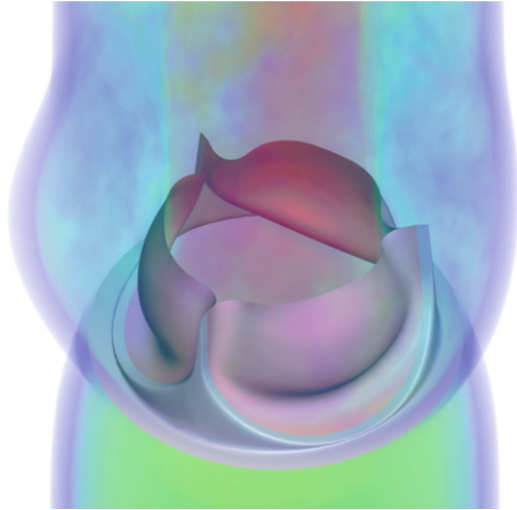
Fig. 18 Snapshots of the valve FSI computation from [77], showing valve deformations and volume renderings of fluid velocity magnitude

6.1 Overview of BHV Simulations

All of the computations reviewed in this section use the VMS discretization of the fluid subproblem described in Sect. 3.1.1 and DAL for fluid–structure coupling. Some of them incorporate phenomena that are beyond the scope of the mathematical problem stated in Sect. 2, such as deforming arteries. However, these BHV simulations illustrate the versatility and practical effectiveness of DAL and IMGGA, so we summarize the results while providing citations for additional details.

We introduced the initial variant of DAL in [77], along with the adjustments to VMS and contact penalty needed to effectively simulate a BHV. A crude BHV model immersed in a rigid artery illustrated the effectiveness of the numerics, although the use of an unrealistic pinned boundary condition on the attached edges of the leaflets led to qualitatively incorrect deformations. Further, the rigid artery and resistance outflow boundary condition provided no hydraulic compliance, causing an abnormal flow rate history [77, Figure 28]. Some snapshots of the valve deformations and velocity fields are rendered in Fig. 18.

Fig. 19 Snapshot of the valve FSI computation from [132], showing valve deformation and volume rendering of fluid velocity magnitude



The model of [77] was augmented with hydraulic compliance in a follow-up publication [130], by modeling the artery wall as an elastic solid. Unlike the immersed valve, the fluid–artery interface was discretized with a boundary-fitted method, which is a special case of FSITICT [123, 131]. The compliance of the elastic artery led to more realistic flow rates [130, Figure 8].

Hsu et al. [132] realized the potential of IMGA to streamline the design-through-analysis process for BHVs. A parametric design-through-analysis framework was used to generate an analysis-suitable T-spline [133] model of a BHV and IMGA allowed for the BHV design geometry to be directly immersed into a discretization of an artery and lumen. The BHV model incorporated a realistic stent geometry, clamped boundary conditions representative of typical industrial BHVs (cf. patent illustrations in [134]), and a soft tissue constitutive model. A snapshot of the resulting BHV FSI simulation is shown in Fig. 19.

6.2 *Div-conforming BHV Simulation*

We now look at a BHV simulation using div-conforming B-splines in the fluid subproblem. A capability that is not verified by the div-conforming FSI benchmark testing in Sect. 5.4 is effective simulation of closing heart valves. In principle, div-conforming B-splines should prevent mass loss altogether, but, in practice, for 3D problems, one generally does not solve the discrete algebraic problem exactly, calling this result into question.

6.2.1 **Test Problem Definition**

A variant of the BHV geometry constructed in [77, Section 5.1] is immersed in a cylindrical fluid domain of radius 1.25 cm and height 3 cm. Rigid extensions are

added to the leaflets, blocking flow passing around the attached boundaries of the leaflets. The fluid subproblem posed on the cylindrical domain has traction boundary conditions on the ends and no-slip and no-penetration conditions on the sides. The bottom of the cylinder is subject to a time-dependent flux condition $\mathbf{h}_1 = P(t)\mathbf{e}_3$, with

$$P(t) = \begin{cases} P_1 & t < T_1 \\ at + b & T_1 \leq t \leq T_2 \\ P_2 & t > T_2 \end{cases} . \quad (57)$$

$P_1 = 2 \times 10^4$ dyn/cm², $T_1 = 0.05$ s, $P_2 = -10^5$ dyn/cm², $T_2 = 0.1$ s, $a = (P_2 - P_1)/(T_2 - T_1)$, and $b = P_1 - aT_1$. The top face is subject to the Neumann condition $\mathbf{h}_1 = \mathbf{0}$. The Neumann boundary stabilization is set to $\gamma = 1$. Properties of the fluid are $\rho_1 = 1$ g/cm³ and $\mu = 4$ cP. The valve is modeled as an incompressible neo-Hookean material with shear modulus $\mu_s = 600$ kPa and density $\rho_2 = 1$ g/cm³. The shell thickness is $h_{\text{th}} = 0.04$ cm. The attached edges of the leaflets are subject to a clamped boundary condition. The fluid and structure are initially at rest at time $t = 0$. This problem is not intended to be a realistic FSI model of a BHV, but rather to exhibit the similar flow conditions, and demonstrate robustness of div-conforming B-splines.

6.2.2 Discretization

The cylindrical fluid domain is discretized using a B-spline knot space $\widehat{\Omega}_1 = [-1, 1]^2 \times [-1, 2]$. A point \mathbf{X} in this knot space is mapped to the physical domain Ω_1 by

$$\phi_1 = RX_1\sqrt{1 - \frac{1}{2}X_2^2}, \quad \phi_2 = RX_2\sqrt{1 - \frac{1}{2}X_1^2}, \quad \phi_3 = LX_3, \quad (58)$$

with $R = 1.25$ cm and $L = 1$ cm. The knot space is evenly subdivided into $42 \times 42 \times 40$ knot spans and div-conforming B-spline velocity and pressure spaces of degree $k' = 1$ are defined on this mesh. The no-penetration constraint on the sides of the cylinder is enforced strongly and the no-slip condition is enforced weakly by velocity penalization, with penalty $C_{\text{no slip}} = 10$ dyn/cm²/(cm/s). Penalty values are $\tau_{\text{NOR}}^B = 1000$ dyn/cm²/(cm/s), $\tau_{\text{TAN}}^B = 10$ dyn/cm²/(cm/s), and $r = 0$. The backward Euler method is used in time with $\Delta t = 5.0 \times 10^{-4}$ s.

6.2.3 Results

The valve opening is illustrated in Fig. 20. The closed state is shown in Fig. 21. The flow rate history through the bottom of the cylinder is given in Fig. 22, indicating that the valve blocks flow. These results illustrate the basic soundness of

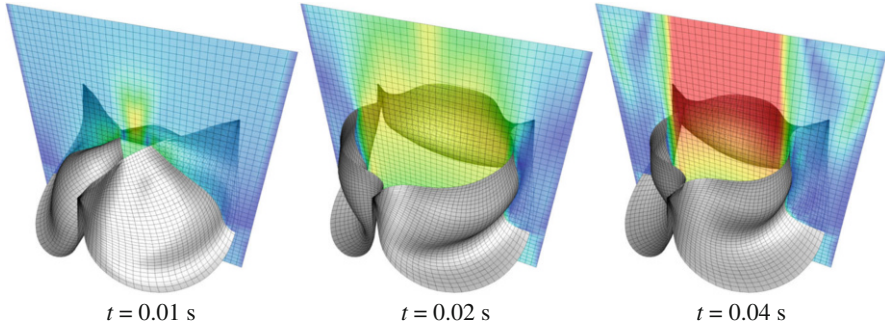
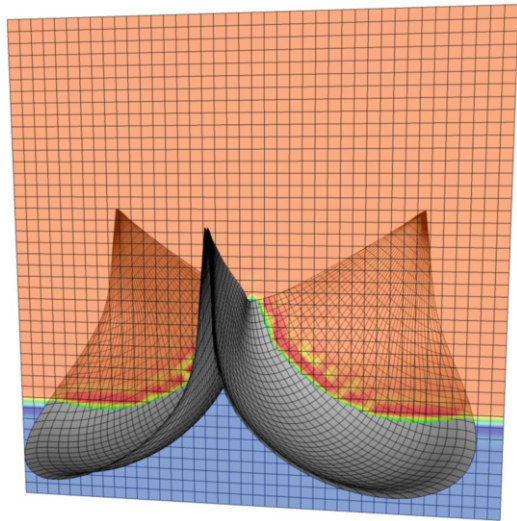


Fig. 20 Velocity magnitude is plotted on a slice, using a color scale ranging from 0 (blue) to ≥ 200 cm/s (red)

Fig. 21 Pressure is plotted on a slice, using a color scale ranging from $\leq -1.1 \times 10^5$ dyn/cm² (blue) to $\geq 10^4$ dyn/cm² (red)



using div-conforming B-splines as a fluid discretization for BHV FSI simulations. We now take a closer look at the mass conservation in the computed solutions. Because we use an iterative solver to approximate the fluid increments in the block iteration, $\nabla \cdot \mathbf{u}_1^h$ is not exactly zero. For the results presented above, we solve for fluid increments with a Krylov method, to a relative tolerance of 10^{-2} for the preconditioned residual. Even with this loose tolerance, there is no disastrous mass loss. We now recompute one step at a time when the valve is closed, under a large pressure jump, with a range of relative tolerances. For this experiment, we use the un-preconditioned residual to measure convergence, so that results generalize more readily to other iterative solvers. The residual is assembled in centimeter–gram–second (CGS) units, without any scaling to compensate for the difference in units between entries of the momentum and continuity equation residuals. The velocity

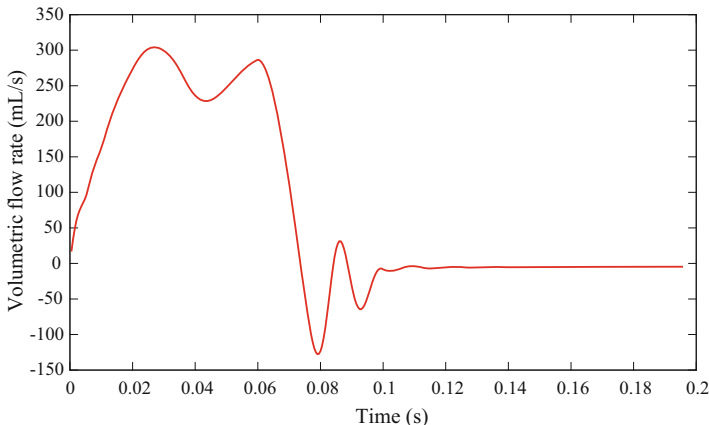


Fig. 22 The volumetric flow rate through the cylinder

Table 1 The effect of relative tolerance in the approximate inversion of A_f on mass conservation

Solver tolerance	$\ \nabla \cdot \mathbf{u}_1\ _{L^2(\Omega_1)}$ (CGS units)
10^{-1}	3.9×10^{-5}
10^{-2}	1.2×10^{-5}
10^{-3}	3.0×10^{-7}
10^{-4}	2.0×10^{-8}
10^{-5}	1.2×10^{-9}
10^{-6}	2.4×10^{-10}
10^{-7}	4.3×10^{-11}

divergence L^2 norms of the solutions to this time step are collected in Table 1. As expected, velocity divergence approaches zero as the tolerance decreases.

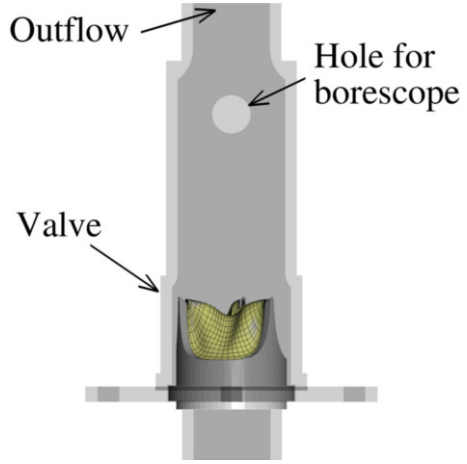
6.3 Simulating an In Vitro Experiment

This section serves both to further illustrate the application of div-conforming B-splines to realistic problems and to argue that the modeling assumptions from Sect. 2 can represent the dynamics of an artificial heart valve immersed in fluid, by summarizing the validation effort detailed in [86, Section 7].

6.3.1 Description of the Experiment

The validation experiment uses a latex valve in an acrylic tube. We constructed the valve by gluing latex leaflets to an aluminum stent. Leaflet are cut from a flat sheet of latex with thickness 0.054 cm. The valve is shown in Fig. 24. The acrylic tube, illustrated in Fig. 23, has an inner diameter varying between 2 and 3 cm along the

Fig. 23 A to-scale diagram of the tube, showing its relation to the valve and stent



length of the tube, and is roughly the size of a typical human ascending aorta. A hole is included in the side of the tube, for capturing images with a borescope.

Water is pumped through the tube using a flow loop system similar to the bioreactor detailed in [135]. Volumetric flow rate through the tube is measured using an ultrasonic flow meter. We use the IMGA with DAL and div-conforming B-splines to simulate only the segment of tubing containing the artificial aortic valve.

6.3.2 Mathematical Model of the Experiment

This section specifies an instance of the mathematical problem stated in Sect. 2 that models the experiment described in Sect. 6.3.1.

Fluid Subproblem

The mathematical model simplifies the geometry of the region occupied by fluid. Ω_1 is the image of a parametric space $\widehat{\Omega}_1 = (-1, 1)^2 \times (-1, 4.5) \subset \mathbb{R}^3$ under the mapping ϕ , which is defined by

$$\phi_1 = R(X_3)X_1\sqrt{1 - \frac{1}{2}X_2^2}, \quad \phi_2 = R(X_3)X_2\sqrt{1 - \frac{1}{2}X_1^2}, \quad \phi_3 = LX_3, \quad (59)$$

where $L = 1$ cm and $R(X_3)$ is defined by

$$R(X_3) = \begin{cases} R_{\text{in}} & X_3 < z_1 \\ R_{\text{out}} & X_3 > z_2 \\ (R_{\text{out}} - R_{\text{in}})\sin^2\left(\frac{\pi(X_3 - z_1)}{2(z_2 - z_1)}\right) + R_{\text{in}} & \text{otherwise} \end{cases}, \quad (60)$$

with $z_1 = -0.45$ cm, $z_2 = 0$, $R_{\text{in}} = 1$ cm, and $R_{\text{out}} = 1.4025$ cm.

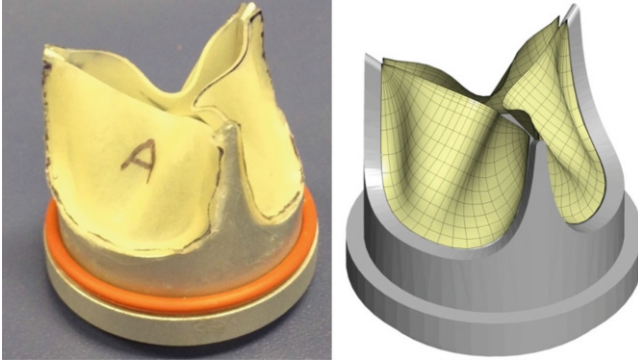


Fig. 24 A visual comparison of the physical valve and its computational model

The lateral sides of Ω_1 are subject to no-slip and no-penetration conditions. The inflow face of the domain is subject to a time-dependent plug flow condition with experimentally measured volumetric flow rate. The outflow is a homogeneous Neumann boundary with $\gamma = 1$. The fluid velocity initial condition is $\mathbf{u}_1^0 \equiv \mathbf{0}$. To model water, the viscosity of the fluid is $\mu = 1$ cP and the density is $\rho_1 = 1.0$ g/cm³.

Structure Subproblem

The latex leaflets are modeled as incompressible neo-Hookean material with shear modulus $\mu_s = 8.7 \times 10^6$ dyn/cm² (based on uniaxial stretching experiments). The geometry of the stress-free reference configuration Γ_0 is specified by manually selecting B-spline control points to approximate the pattern used to cut the leaflets out of the latex sheet. The leaflets are therefore flat in Γ_0 . These leaflets are deformed into a static equilibrium configuration Γ'_0 , (a discrete approximation of) which is shown in Fig. 24. The boundary corresponding to the attached edge is subject to a strongly enforced clamped boundary condition. In a slight abuse of the notation introduced in Sect. 2, the leaflets are considered to be initially at rest in the deformed configuration Γ'_0 , rather than the stress-free configuration Γ_0 .

6.3.3 Discretization of the Mathematical Model

The fluid parametric domain $\widehat{\Omega}_1$ is split evenly into $64 \times 64 \times 99$ Bézier elements, used to define div-conforming B-spline spaces of degree $k' = 1$. No-slip and inflow Dirichlet boundary conditions are enforced by velocity penalization, with penalty-constants of $C_{\text{no slip}} = 10$ dyn/cm²/(cm/s) and $C_{\text{inflow}} = 1000$ dyn/cm²/(cm/s). No-penetration on the lateral sides of the flow domain is enforced strongly. The structure is discretized with a 936-element quadratic B-spline mesh. The equilibrium configuration Γ'_0 is approximated by driving a dynamic simulation

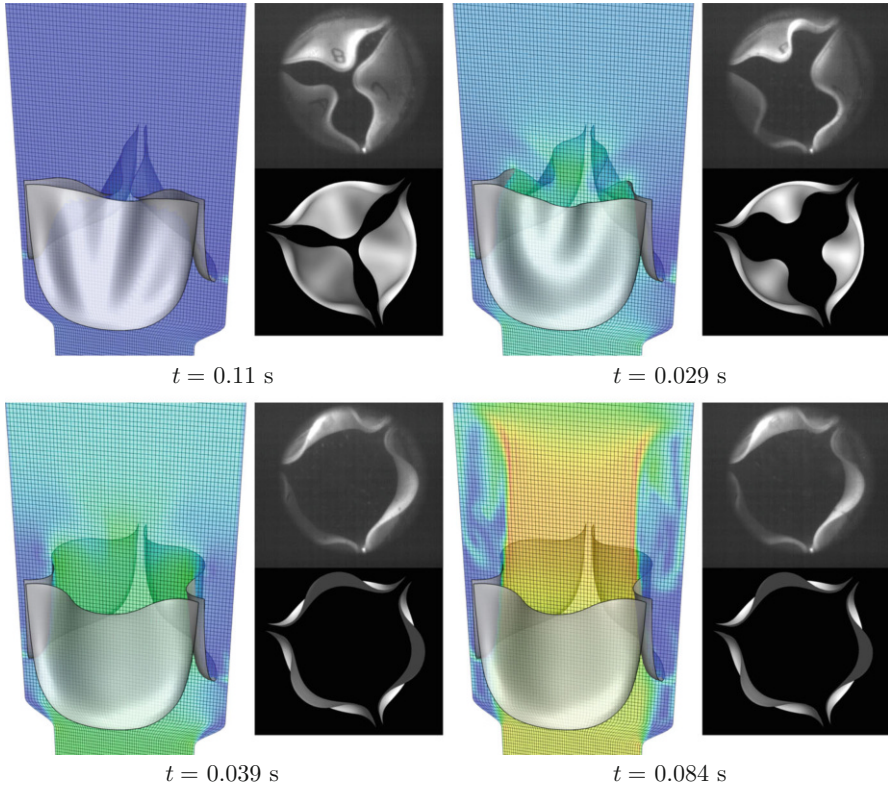


Fig. 25 Several snapshots of the computed solution, compared with experimental images. At each time instant, the computed solution is shown in the left-hand frame and at the bottom of the right-hand frame. The experimental results are shown in the top of the right-hand frame. Colors indicate fluid velocity magnitude on a slice. Color scale: 0 (blue) to ≥ 200 cm/s (red)

with mass damping from Γ_0 to a steady solution. The attached edges of the leaflets are then clamped into this configuration. The FSI penalty parameters are $\tau_{\text{NOR}}^B = 1000 \text{ dyn/cm}^2/(\text{cm/s})$ and $\tau_{\text{TAN}}^B = 10 \text{ dyn/cm}^2/(\text{cm/s})$. The DAL stabilization parameter r is set to zero. Backward Euler time integration is used with $\Delta t = 2.5 \times 10^{-4} \text{ s}$.

6.3.4 Comparison of Results

We now compare computational and experimental results. Experimental results are a sequence of images taken through a borescope. Figure 25 compares the computed deformations at several time points with images collected in the experiment. For direct comparison with experimental images, the computed deformations are rendered using perspective, from a vantage point corresponding to the tip of the borescope in the experiment.

The main qualitative difference between these sets of images is in the degree of symmetry of the leaflet deformations during the transition to the fully open state. This difference is expected, given that the initial condition to the computer simulation is symmetrical while the physical valve is not. Asymmetry is mainly due to experimental errors introduced by manually gluing each initially flat leaflet into the stent. The qualitative agreement of results indicates that the modeling assumptions of Sect. 2 are not wildly inappropriate for predicting the deformations of BHV leaflets immersed in physiological flow fields, and may be able to predict quantities of interest related to deformation (such as strain) with practical accuracy. The computed results also agree with qualitative features of artificial valve leaflet deformations observed in other *in vitro* experiments. The computed solution at time $t = 0.029$ s shows the opening process, as characterized by reversal of leaflet curvature, beginning primarily near the attached edge, as observed by Iyengar et al. [136]. Hsu et al. [132] found that this behavior is *not* captured by simulations using only structural dynamics.

7 Conclusions and Further Work

This chapter reviews the development, verification, and application of a novel numerical method combining IMGGA and DAL to simulate thin structures with spline-based geometries immersed in viscous incompressible fluids. We find that this method is sufficiently robust to survive application to FSI analysis of BHVs functioning under physiological conditions.

The method described here is not limited to BHV simulation. We have also applied it to IMGGA of the hydraulic arresting gears that help dissipate the kinetic energy of fixed-wing aircraft landing on short runways. Initial results, published in [137], compare favorably with earlier body-fitted simulations of such devices [138]. The flexibility provided by immersogeometric FSI analysis allowed for automated optimization of the device geometry.

Despite its successful application to BHV FSI and other problems, the DAL method outlined here can be improved. The present guidelines for selecting free penalty parameters are based on imprecise dimensional analysis. More precise and rational selection of parameters will likely stem from further numerical analysis of linear model problems, building on the initial work of [86]. Another undesirable aspect of the method presented in this dissertation is the trade-off between conservation and stability parameterized by the stabilization coefficient r (introduced in Sect. 4.1). A possible improvement is to apply the inconsistent stabilization of $r > 0$ only to fine scales of the interface Lagrange multiplier, while retaining strong consistency on coarse scales. Initial work on this was published in [139] and is analyzed in a forthcoming paper [140].

Lastly, the promising initial results of immersogeometric FSI analysis using div-conforming B-spline discretizations of the fluid subproblem indicate that div-conforming B-splines merit further investigation. Casquero et al. [141] have also

recently applied div-conforming B-splines in conjunction with the immersed-boundary numerical approach of [142–144] and efficient solvers from [145]. The ideas of immersogeometric FSI analysis and div-conforming B-spline flow discretizations appear to enjoy a symbiotic connection, in that the strong mass conservation of structure preserving flow discretizations improves the quality of immersogeometric FSI solutions, while the application of div-conforming B-splines to increasingly complicated and realistic problems motivates the development of more powerful implementations.

Acknowledgements The work summarized in this chapter was supported by the National Heart, Lung, and Blood Institute of the National Institutes of Health (NIH/NHLBI) under award number R01HL129077. We thank the Texas Advanced Computing Center (TACC) at the University of Texas at Austin for providing HPC resources that have contributed to the research results reported in this chapter.

References

1. F. J. Schoen and R. J. Levy. Calcification of tissue heart valve substitutes: progress toward understanding and prevention. *Ann. Thorac. Surg.*, 79(3):1072–1080, 2005.
2. P. Pibarot and J. G. Dumesnil. Prosthetic heart valves: selection of the optimal prosthesis and long-term management. *Circulation*, 119(7):1034–1048, 2009.
3. J. S. Soares, K. R. Feaver, W. Zhang, D. Kamensky, A. Aggarwal, and M. S. Sacks. Biomechanical behavior of bioprosthetic heart valve heterograft tissues: Characterization, simulation, and performance. *Cardiovascular Engineering and Technology*, 7(4):309–351, 2016.
4. M. J. Thubrikar, J. D. Deck, J. Aouad, and S. P. Nolan. Role of mechanical stress in calcification of aortic bioprosthetic valves. *J. Thorac. Cardiovasc. Surg.*, 86(1):115–125, Jul 1983.
5. R. F. Siddiqui, J. R. Abraham, and J. Butany. Bioprosthetic heart valves: modes of failure. *Histopathology*, 55:135–144, 2009.
6. W. Sun, A. Abad, and M. S. Sacks. Simulated bioprosthetic heart valve deformation under quasi-static loading. *Journal of Biomechanical Engineering*, 127(6):905–914, 2005.
7. F. Auricchio, M. Conti, A. Ferrara, S. Morganti, and A. Reali. Patient-specific simulation of a stentless aortic valve implant: the impact of fibres on leaflet performance. *Computer Methods in Biomechanics and Biomedical Engineering*, 17(3):277–285, 2014.
8. H. Kim, J. Lu, M. S. Sacks, and K. B. Chandran. Dynamic simulation of bioprosthetic heart valves using a stress resultant shell model. *Annals of Biomedical Engineering*, 36(2):262–275, 2008.
9. T. J. R. Hughes, W. K. Liu, and T. K. Zimmermann. Lagrangian–Eulerian finite element formulation for incompressible viscous flows. *Computer Methods in Applied Mechanics and Engineering*, 29:329–349, 1981.
10. J. Donea, S. Giuliani, and J. P. Halleux. An arbitrary Lagrangian–Eulerian finite element method for transient dynamic fluid–structure interactions. *Computer Methods in Applied Mechanics and Engineering*, 33:689–723, 1982.
11. J. Donea, A. Huerta, J.-P. Ponthot, and A. Rodriguez-Ferran. Arbitrary Lagrangian–Eulerian methods. In *Encyclopedia of Computational Mechanics*, Volume 3: Fluids, chapter 14. John Wiley & Sons, 2004.

12. T. E. Tezduyar, M. Behr, and J. Liou. A new strategy for finite element computations involving moving boundaries and interfaces – the deforming-spatial-domain/space–time procedure: I. The concept and the preliminary numerical tests. *Computer Methods in Applied Mechanics and Engineering*, 94(3):339–351, 1992.
13. T. E. Tezduyar, M. Behr, S. Mittal, and J. Liou. A new strategy for finite element computations involving moving boundaries and interfaces – the deforming-spatial-domain/space–time procedure: II. Computation of free-surface flows, two-liquid flows, and flows with drifting cylinders. *Computer Methods in Applied Mechanics and Engineering*, 94(3):353–371, 1992.
14. A. A. Johnson and T. E. Tezduyar. Parallel computation of incompressible flows with complex geometries. *International Journal for Numerical Methods in Fluids*, 24:1321–1340, 1997.
15. T. Tezduyar, S. Aliabadi, M. Behr, A. Johnson, and S. Mittal. Massively parallel finite element computation of 3D flows – mesh update strategies in computation of moving boundaries and interfaces. In A. Ecer, J. Hauser, P. Leca, and J. Periaux, editors, *Parallel Computational Fluid Dynamics – New Trends and Advances*, pages 21–30. Elsevier, 1995.
16. A. A. Johnson and T. E. Tezduyar. 3D simulation of fluid-particle interactions with the number of particles reaching 100. *Computer Methods in Applied Mechanics and Engineering*, 145:301–321, 1997.
17. A. A. Johnson and T. E. Tezduyar. Advanced mesh generation and update methods for 3D flow simulations. *Computational Mechanics*, 23:130–143, 1999.
18. K. Takizawa, T. E. Tezduyar, A. Buscher, and S. Asada. Space–time interface-tracking with topology change (ST-TC). *Computational Mechanics*, 54:955–971, 2014.
19. K. Takizawa, T. E. Tezduyar, A. Buscher, and S. Asada. Space–time fluid mechanics computation of heart valve models. *Computational Mechanics*, 54:973–986, 2014.
20. K. Takizawa, T. E. Tezduyar, T. Terahara, and T. Sasaki. Heart valve flow computation with the integrated space–time VMS, slip interface, topology change and isogeometric discretization methods. *Computers & Fluids*, 158:176–188, 2017.
21. K. Takizawa, T. E. Tezduyar, T. Terahara, and T. Sasaki. Heart valve flow computation with the space–time slip interface topology change (ST-SI-TC) method and isogeometric analysis (IGA). In P. Wriggers and T. Lenarz, editors, *Biomedical Technology: Modeling, Experiments and Simulation*, Lecture Notes in Applied and Computational Mechanics, pages 77–99. Springer International Publishing, 2018.
22. C. S. Peskin. Flow patterns around heart valves: A numerical method. *Journal of Computational Physics*, 10(2):252–271, 1972.
23. R. Mittal and G. Iaccarino. Immersed boundary methods. *Annual Review of Fluid Mechanics*, 37:239–261, 2005.
24. F. Sotiropoulos and X. Yang. Immersed boundary methods for simulating fluid–structure interaction. *Progress in Aerospace Sciences*, 65:1–21, 2014.
25. D. Schillinger, L. Dedè, M. A. Scott, J. A. Evans, M. J. Borden, E. Rank, and T. J. R. Hughes. An isogeometric design-through-analysis methodology based on adaptive hierarchical refinement of NURBS, immersed boundary methods, and T-spline CAD surfaces. *Computer Methods in Applied Mechanics and Engineering*, 249–252:116–150, 2012.
26. T. E. Tezduyar. Computation of moving boundaries and interfaces and stabilization parameters. *International Journal for Numerical Methods in Fluids*, 43:555–575, 2003.
27. K. Takizawa, C. Moorman, S. Wright, J. Christopher, and T. E. Tezduyar. Wall shear stress calculations in space–time finite element computation of arterial fluid–structure interactions. *Computational Mechanics*, 46:31–41, 2010.
28. J. de Hart. *Fluid–Structure Interaction in the Aortic Heart Valve: a three-dimensional computational analysis*. Ph.D. thesis, Technische Universiteit Eindhoven, Eindhoven, Netherlands, 2002.
29. J. De Hart, G. W. M. Peters, P. J. G. Schreurs, and F. P. T. Baaijens. A three-dimensional computational analysis of fluid–structure interaction in the aortic valve. *Journal of Biomechanics*, 36:103–112, 2003.

30. J. De Hart, F. P. T. Baaijens, G. W. M. Peters, and P. J. G. Schreurs. A computational fluid–structure interaction analysis of a fiber-reinforced stentless aortic valve. *Journal of Biomechanics*, 36:699–712, 2003.
31. R. van Loon. *A 3D method for modelling the fluid–structure interaction of heart valves*. Ph.D. thesis, Technische Universiteit Eindhoven, Eindhoven, Netherlands, 2005.
32. R. van Loon, P. D. Anderson, and F. N. van de Vosse. A fluid–structure interaction method with solid-rigid contact for heart valve dynamics. *Journal of Computational Physics*, 217:806–823, 2006.
33. R. van Loon. Towards computational modelling of aortic stenosis. *International Journal for Numerical Methods in Biomedical Engineering*, 26:405–420, 2010.
34. F. P. T. Baaijens. A fictitious domain/mortar element method for fluid–structure interaction. *International Journal for Numerical Methods in Fluids*, 35(7):743–761, 2001.
35. B. E. Griffith. Immersed boundary model of aortic heart valve dynamics with physiological driving and loading conditions. *International Journal for Numerical Methods in Biomedical Engineering*, 28(3):317–345, 2012.
36. I. Borazjani. Fluid–structure interaction, immersed boundary-finite element method simulations of bio-prosthetic heart valves. *Computer Methods in Applied Mechanics and Engineering*, 257:103–116, 2013.
37. L. Ge and F. Sotiropoulos. A numerical method for solving the 3D unsteady incompressible Navier–Stokes equations in curvilinear domains with complex immersed boundaries. *Journal of Computational Physics*, 225(2):1782–1809, 2007.
38. I. Borazjani, L. Ge, and F. Sotiropoulos. Curvilinear immersed boundary method for simulating fluid structure interaction with complex 3D rigid bodies. *Journal of Computational Physics*, 227(16):7587–7620, 2008.
39. A. Gilmanov, T. B. Le, and F. Sotiropoulos. A numerical approach for simulating fluid structure interaction of flexible thin shells undergoing arbitrarily large deformations in complex domains. *Journal of Computational Physics*, 300:814–843, 2015.
40. A. Gilmanov and F. Sotiropoulos. Comparative hemodynamics in an aorta with bicuspid and trileaflet valves. *Theoretical and Computational Fluid Dynamics*, 30(1):67–85, 2016.
41. LS-DYNA Finite Element Software: Livermore Software Technology Corp. <http://www.lstc.com/products/ls-dyna>. Accessed 30 April 2016.
42. G. G. Chew, I. C. Howard, and E. A. Patterson. Simulation of damage in a porcine prosthetic heart valve. *Journal of Medical Engineering & Technology*, 23(5):178–189, 1999.
43. C. J. Carmody, G. Burriesci, I. C. Howard, and E. A. Patterson. An approach to the simulation of fluid–structure interaction in the aortic valve. *Journal of Biomechanics*, 39:158–169, 2006.
44. F. Sturla, E. Votta, M. Stevanella, C. A. Conti, and A. Redaelli. Impact of modeling fluid–structure interaction in the computational analysis of aortic root biomechanics. *Medical Engineering and Physics*, 35:1721–1730, 2013.
45. W. Wu, D. Pott, B. Mazza, T. Sironi, E. Dordoni, C. Chiastra, L. Petrini, G. Pennati, G. Dubini, U. Steinseifer, S. Sonntag, M. Kuetting, and F. Migliavacca. Fluid–structure interaction model of a percutaneous aortic valve: Comparison with an in vitro test and feasibility study in a patient-specific case. *Annals of Biomedical Engineering*, 44(2):590–603, 2016.
46. R. Courant, K. Friedrichs, and H. Lewy. Über die partiellen Differenzgleichungen der mathematischen Physik. *Mathematische Annalen*, 100(1):32–74, 1928.
47. R. Courant, K. Friedrichs, and H. Lewy. On the partial difference equations of mathematical physics. *IBM J. Res. Develop.*, 11:215–234, 1967.
48. A. E. J. Bogaers, S. Kok, B. D. Reddy, and T. Franz. Quasi-Newton methods for implicit black-box FSI coupling. *Computer Methods in Applied Mechanics and Engineering*, 279(0):113–132, 2014.
49. E. H. van Brummelen. Added mass effects of compressible and incompressible flows in fluid–structure interaction. *Journal of Applied Mechanics*, 76:021206, 2009.
50. C. Michler, H. van Brummelen, and R. de Borst. An investigation of interface-GMRES(R) for fluid–structure interaction problems with flutter and divergence. *Computational Mechanics*, 47(1):17–29, 2011.

51. M. Astorino, J.-F. Gerbeau, O. Pantz, and K.-F. Traoré. Fluid–structure interaction and multi-body contact: Application to aortic valves. *Computer Methods in Applied Mechanics and Engineering*, 198:3603–3612, 2009.
52. K. Cao, M. Bukač, and P. Sucusky. Three-dimensional macro-scale assessment of regional and temporal wall shear stress characteristics on aortic valve leaflets. *Computer Methods in Biomechanics and Biomedical Engineering*, 19(6):603–613, 2016.
53. T. J. R. Hughes, J. A. Cottrell, and Y. Bazilevs. Isogeometric analysis: CAD, finite elements, NURBS, exact geometry and mesh refinement. *Computer Methods in Applied Mechanics and Engineering*, 194:4135–4195, 2005.
54. J. A. Evans, Y. Bazilevs, I. Babuška, and T. J. R. Hughes. n -Widths, sup-infs, and optimality ratios for the k -version of the isogeometric finite element method. *Computer Methods in Applied Mechanics and Engineering*, 198:1726–1741, 2009.
55. A. Buffa, G. Sangalli, and R. Vázquez. Isogeometric analysis in electromagnetics: B-splines approximation. *Computer Methods in Applied Mechanics and Engineering*, 199(17–20):1143–1152, 2010.
56. A. Buffa, J. Rivas, G. Sangalli, and R. Vázquez. Isogeometric discrete differential forms in three dimensions. *SIAM Journal on Numerical Analysis*, 49(2):814–844, 2011.
57. I. Akkerman, Y. Bazilevs, V. M. Calo, T. J. R. Hughes, and S. Hulshoff. The role of continuity in residual-based variational multiscale modeling of turbulence. *Computational Mechanics*, 41:371–378, 2008.
58. Y. Bazilevs, V. M. Calo, J. A. Cottrell, T. J. R. Hughes, A. Reali, and G. Scovazzi. Variational multiscale residual-based turbulence modeling for large eddy simulation of incompressible flows. *Computer Methods in Applied Mechanics and Engineering*, 197:173–201, 2007.
59. J. A. Evans. *Divergence-free B-spline Discretizations for Viscous Incompressible Flows*. Ph.D. thesis, University of Texas at Austin, Austin, Texas, United States, 2011.
60. J. A. Evans and T. J. R. Hughes. Isogeometric divergence-conforming B-splines for the steady Navier–Stokes equations. *Mathematical Models and Methods in Applied Sciences*, 23(08):1421–1478, 2013.
61. J. Kiendl, K.-U. Bletzinger, J. Linhard, and R. Wüchner. Isogeometric shell analysis with Kirchhoff–Love elements. *Computer Methods in Applied Mechanics and Engineering*, 198:3902–3914, 2009.
62. J. Kiendl. *Isogeometric Analysis and Shape Optimal Design of Shell Structures*. PhD thesis, Lehrstuhl für Statik, Technische Universität München, 2011.
63. N. Nguyen-Thanh, J. Kiendl, H. Nguyen-Xuan, R. Wüchner, K.U. Bletzinger, Y. Bazilevs, and T. Rabczuk. Rotation-free isogeometric thin shell analysis using PHT-splines. *Computer Methods in Applied Mechanics and Engineering*, 200:3410–3424, 2011.
64. J. Kiendl, M.-C. Hsu, M. C. H. Wu, and A. Reali. Isogeometric Kirchhoff–Love shell formulations for general hyperelastic materials. *Computer Methods in Applied Mechanics and Engineering*, 291:280–303, 2015.
65. S. Lipton, J. A. Evans, Y. Bazilevs, T. Elguedj, and T. J. R. Hughes. Robustness of isogeometric structural discretizations under severe mesh distortion. *Computer Methods in Applied Mechanics and Engineering*, 199:357–373, 2010.
66. L. De Lorenzis, Í. Temizer, P. Wriggers, and G. Zavarise. A large deformation frictional contact formulation using NURBS-based isogeometric analysis. *International Journal for Numerical Methods in Engineering*, 87:1278–1300, 2011.
67. S. Morganti, F. Auricchio, D. J. Benson, F. I. Gambarin, S. Hartmann, T. J. R. Hughes, and A. Reali. Patient-specific isogeometric structural analysis of aortic valve closure. *Computer Methods in Applied Mechanics and Engineering*, 284:508–520, 2015.
68. M. A. Scott. *T-splines as a Design-Through-Analysis Technology*. PhD thesis, The University of Texas at Austin, August 2011.
69. T. W. Sederberg, D.L. Cardon, G.T. Finnigan, N.S. North, J. Zheng, and T. Lyche. T-spline simplification and local refinement. *ACM Transactions on Graphics*, 23(3):276–283, 2004.
70. T.W. Sederberg, J. Zheng, A. Bakenov, and A. Nasri. T-splines and T-NURCCS. *ACM Transactions on Graphics*, 22(3):477–484, 2003.

71. E. Rank, M. Ruess, S. Kollmannsberger, D. Schillinger, and A. Düster. Geometric modeling, isogeometric analysis and the finite cell method. *Computer Methods in Applied Mechanics and Engineering*, 249–252:104–115, 2012.
72. M. Ruess, D. Schillinger, Y. Bazilevs, V. Varduhn, and E. Rank. Weakly enforced essential boundary conditions for NURBS-embedded and trimmed NURBS geometries on the basis of the finite cell method. *International Journal for Numerical Methods in Engineering*, 95:811–846, 2013.
73. M. Ruess, D. Schillinger, A. I. Özcan, and E. Rank. Weak coupling for isogeometric analysis of non-matching and trimmed multi-patch geometries. *Computer Methods in Applied Mechanics and Engineering*, 269:46–731, 2014.
74. D. Schillinger and M. Ruess. The Finite Cell Method: A review in the context of higher-order structural analysis of CAD and image-based geometric models. *Archives of Computational Methods in Engineering*, 22(3):391–455, 2015.
75. D. Schillinger, M. Ruess, N. Zander, Y. Bazilevs, A. Düster, and E. Rank. Small and large deformation analysis with the p - and B-spline versions of the Finite Cell Method. *Computational Mechanics*, 50(4):445–478, 2012.
76. G. Strang and G. J. Fix. *An Analysis of the Finite Element Method*. Prentice-Hall, Englewood Cliffs, New Jersey, 1973.
77. D. Kamensky, M.-C. Hsu, D. Schillinger, J. A. Evans, A. Aggarwal, Y. Bazilevs, M. S. Sacks, and T. J. R. Hughes. An immersogeometric variational framework for fluid–structure interaction: Application to bioprosthetic heart valves. *Computer Methods in Applied Mechanics and Engineering*, 284:1005–1053, 2015.
78. M. Hillairet. Lack of collision between solid bodies in a 2D incompressible viscous flow. *Communications in Partial Differential Equations*, 32(9):1345–1371, 2007.
79. Y. Bazilevs, M.-C. Hsu, and M. A. Scott. Isogeometric fluid–structure interaction analysis with emphasis on non-matching discretizations, and with application to wind turbines. *Computer Methods in Applied Mechanics and Engineering*, 249–252:28–41, 2012.
80. M. Esmaily-Moghadam, Y. Bazilevs, T.-Y. Hsia, I. E. Vignon-Clementel, A. L. Marsden, and Modeling of Congenital Hearts Alliance (MOCHA). A comparison of outlet boundary treatments for prevention of backflow divergence with relevance to blood flow simulations. *Computational Mechanics*, 48:277–291, 2011.
81. G. A. Holzapfel. *Nonlinear Solid Mechanics: A Continuum Approach for Engineering*. Wiley, Chichester, 2000.
82. T. M. van Opstal, J. Yan, C. Coley, J. A. Evans, T. Kvamsdal, and Y. Bazilevs. Isogeometric divergence-conforming variational multiscale formulation of incompressible turbulent flows. *Computer Methods in Applied Mechanics and Engineering*, 316:859–879, 2017.
83. T. J. R. Hughes, G. R. Feijóo, L. Mazzei, and J. B. Quincy. The variational multiscale method—A paradigm for computational mechanics. *Computer Methods in Applied Mechanics and Engineering*, 166:3–24, 1998.
84. S. C. Brenner and L. R. Scott. *The Mathematical Theory of Finite Element Methods, 3rd ed.* Springer, 2008.
85. J. A. Evans and T. J. R. Hughes. Explicit trace inequalities for isogeometric analysis and parametric hexahedral finite elements. *Numerische Mathematik*, 123:259–290, 2013.
86. D. Kamensky, M.-C. Hsu, Y. Yu, J. A. Evans, M. S. Sacks, and T. J. R. Hughes. Immer- sogeometric cardiovascular fluid–structure interaction analysis with divergence-conforming B-splines. *Computer Methods in Applied Mechanics and Engineering*, 314:408–472, 2017.
87. J. A. Evans and T. J. R. Hughes. Isogeometric divergence-conforming B-splines for the unsteady Navier–Stokes equations. *Journal of Computational Physics*, 241:141–167, 2013.
88. L. Piegl and W. Tiller. *The NURBS Book (Monographs in Visual Communication), 2nd ed.* Springer-Verlag, New York, 1997.
89. A. N. Brooks and T. J. R. Hughes. Streamline upwind/Petrov-Galerkin formulations for convection dominated flows with particular emphasis on the incompressible Navier-Stokes equations. *Computer Methods in Applied Mechanics and Engineering*, 32:199–259, 1982.

90. Y. Bazilevs and T. J. R. Hughes. Weak imposition of Dirichlet boundary conditions in fluid mechanics. *Computers and Fluids*, 36:12–26, 2007.
91. Y. Bazilevs, C. Michler, V. M. Calo, and T. J. R. Hughes. Weak Dirichlet boundary conditions for wall-bounded turbulent flows. *Computer Methods in Applied Mechanics and Engineering*, 196:4853–4862, 2007.
92. Y. Bazilevs, C. Michler, V. M. Calo, and T. J. R. Hughes. Isogeometric variational multiscale modeling of wall-bounded turbulent flows with weakly enforced boundary conditions on unstretched meshes. *Computer Methods in Applied Mechanics and Engineering*, 199:780–790, 2010.
93. Y. Bazilevs and I. Akkerman. Large eddy simulation of turbulent Taylor–Couette flow using isogeometric analysis and the residual–based variational multiscale method. *Journal of Computational Physics*, 229:3402–3414, 2010.
94. M.-C. Hsu, I. Akkerman, and Y. Bazilevs. Wind turbine aerodynamics using ALE–VMS: Validation and the role of weakly enforced boundary conditions. *Computational Mechanics*, 50:499–511, 2012.
95. H. J. C. Barbosa and T. J. R. Hughes. The finite element method with Lagrange multipliers on the boundary: circumventing the Babuška–Brezzi condition. *Computer Methods in Applied Mechanics and Engineering*, 85(1):109–128, 1991.
96. J. Chung and G. M. Hulbert. A time integration algorithm for structural dynamics with improved numerical dissipation: The generalized- α method. *Journal of Applied Mechanics*, 60:371–75, 1993.
97. Y. Bazilevs, V. M. Calo, T. J. R. Hughes, and Y. Zhang. Isogeometric fluid–structure interaction: theory, algorithms, and computations. *Computational Mechanics*, 43:3–37, 2008.
98. M. R. Hestenes. Multiplier and gradient methods. *Journal of Optimization Theory and Applications*, 4(5):303–320, 1969.
99. M. J. D. Powell. A method for nonlinear constraints in minimization problems. In R. Fletcher, editor, *Optimization*, pages 283–298. Academic Press, New York, 1969.
100. D. Kamensky, J. A. Evans, and M.-C. Hsu. Stability and conservation properties of collocated constraints in immersogeometric fluid–thin structure interaction analysis. *Communications in Computational Physics*, 18:1147–1180, 2015.
101. A. J. Chorin. A numerical method for solving incompressible viscous flow problems. *Journal of Computational Physics*, 135(2):118–125, 1967.
102. D. Goldstein, R. Handler, and L. Sirovich. Modeling a no-slip flow boundary with an external force field. *Journal of Computational Physics*, 105(2):354–366, 1993.
103. L. B. Wahlbin. Local behavior in finite element methods. In P. G. Ciarlet and J. L. Lions, editors, *Finite Element Methods (Part 1)*, volume 2 of *Handbook of Numerical Analysis*, pages 353–522. North-Holland, 1991.
104. T.-C. Tuan and D. B. Goldstein. Direct numerical simulation of arrays of microjets to manipulate near wall turbulence. Technical Report CAR-96-3, U. T. Austin Center for Aerodynamics Research, 2011.
105. D. B. Goldstein and T.-C. Tuan. Secondary flow induced by riblets. *Journal of Fluid Mechanics*, 363:115–151, 1998.
106. D. B. Goldstein. DNS for new applications of surface textures and MEMS actuators for turbulent boundary layer control - FINAL REPORT. Technical Report AFRL-SR-AR-TR-07-0363, AFSOR, 2006.
107. K. Stephani and D. Goldstein. DNS study of transient disturbance growth and bypass transition due to realistic roughness. In *Proceedings of 47th AIAA Aerospace Sciences Meeting including The New Horizons Forum and Aerospace Exposition*, AIAA Paper 2009-585, Orlando, Florida, 2009.
108. J. S. Strand and D. B. Goldstein. Direct numerical simulations of riblets to constrain the growth of turbulent spots. *Journal of Fluid Mechanics*, 668:267–292, 2011.
109. C. J. Doolittle, S. D. Drews, and D. B. Goldstein. Near-field flow structures about subcritical surface roughness. *Physics of Fluids*, 26:124106, 2014.

110. E. M. Saiki and S. Biringen. Numerical simulation of a cylinder in uniform flow: Application of a virtual boundary method. *Journal of Computational Physics*, 123(2):450–465, 1996.
111. E. M. Saiki and S. Biringen. Spatial numerical simulation of boundary layer transition: effects of a spherical particle. *Journal of Fluid Mechanics*, 345:133–164, 1997.
112. W.-X. Huang, S. J. Shin, and H. J. Sung. Simulation of flexible filaments in a uniform flow by the immersed boundary method. *Journal of Computational Physics*, 226(2):2206–2228, 2007.
113. S. J. Shin, W.-X. Huang, and H. J. Sung. Assessment of regularized delta functions and feedback forcing schemes for an immersed boundary method. *International Journal for Numerical Methods in Fluids*, 58(3):263–286, 2008.
114. W.-X. Huang and H. J. Sung. An immersed boundary method for fluid–flexible structure interaction. *Computer Methods in Applied Mechanics and Engineering*, 198(33–36):2650–2661, 2009.
115. J. Ryu, S. G. Park, B. Kim, and H. J. Sung. Flapping dynamics of an inverted flag in a uniform flow. *Journal of Fluids and Structures*, 57:159–169, 2015.
116. E. Uddin, W.-X. Huang, and H. J. Sung. Actively flapping tandem flexible flags in a viscous flow. *Journal of Fluid Mechanics*, 780:120–142, 10 2015.
117. M. Souli, Y. Sofiane, and L. Olovsson. ALE and fluid/structure interaction in LS-DYNA. In *Proceedings of Emerging Technology in Fluids, Structures, and Fluid–Structure Interactions*. ASME, 2004.
118. M. Souli, N. Capron, and U. Khan. Fluid structure interaction and airbag ALE for out of position. In *Proceedings of the ASME Pressure Vessels and Piping Conference*. AMSE, 2005.
119. M. Souli, J. Wang, I. Do, and C. Hao. ALE and fluid structure interaction in LS-DYNA. In *Proceedings of the 8th International LS-DYNA Users Conference*, 2011.
120. A. Haufe, K. Weimar, and U. Göhner. Advanced airbag simulation using fluid-structure-interaction and the Eluerian method in LS-DYNA. In *Proceedings of the LS-DYNA Anwenderforum*, 2004.
121. A. J. Gil, A. Arranz Carreño, J. Bonet, and O. Hassan. An enhanced immersed structural potential method for fluid–structure interaction. *Journal of Computational Physics*, 250:178–205, 2013.
122. C. Hesch, A. J. Gil, A. Arranz Carreño, and J. Bonet. On continuum immersed strategies for fluid-structure interaction. *Computer Methods in Applied Mechanics and Engineering*, 247–248:51–64, 2012.
123. T. Wick. Flapping and contact FSI computations with the fluid–solid interface-tracking/interface-capturing technique and mesh adaptivity. *Computational Mechanics*, 53(1):29–43, 2014.
124. C. Kadapa, W. G. Dettmer, and D. Perić. A fictitious domain/distributed Lagrange multiplier based fluid–structure interaction scheme with hierarchical B-spline grids. *Computer Methods in Applied Mechanics and Engineering*, 301:1–27, 2016.
125. T. Tezduyar, S. Aliabadi, M. Behr, A. Johnson, and S. Mittal. Parallel finite-element computation of 3D flows. *Computer*, 26(10):27–36, 1993.
126. A. A. Johnson and T. E. Tezduyar. Mesh update strategies in parallel finite element computations of flow problems with moving boundaries and interfaces. *Computer Methods in Applied Mechanics and Engineering*, 119:73–94, 1994.
127. K. Stein, T. Tezduyar, and R. Benney. Mesh moving techniques for fluid–structure interactions with large displacements. *Journal of Applied Mechanics*, 70:58–63, 2003.
128. K. Stein, T. E. Tezduyar, and R. Benney. Automatic mesh update with the solid-extension mesh moving technique. *Computer Methods in Applied Mechanics and Engineering*, 193:2019–2032, 2004.
129. Y. Bazilevs, K. Takizawa, and T. E. Tezduyar. *Computational Fluid–Structure Interaction: Methods and Applications*. Wiley, Chichester, 2013.
130. M.-C. Hsu, D. Kamensky, Y. Bazilevs, M. S. Sacks, and T. J. R. Hughes. Fluid–structure interaction analysis of bioprosthetic heart valves: significance of arterial wall deformation. *Computational Mechanics*, 54:1055–1071, 2014.

131. T. E. Tezduyar, K. Takizawa, C. Moorman, S. Wright, and J. Christopher. Space–time finite element computation of complex fluid–structure interactions. *International Journal for Numerical Methods in Fluids*, 64:1201–1218, 2010.
132. M.-C. Hsu, D. Kamensky, F. Xu, J. Kiendl, C. Wang, M. C. H. Wu, J. Mineroff, A. Reali, Y. Bazilevs, and M. S. Sacks. Dynamic and fluid–structure interaction simulations of bioprosthetic heart valves using parametric design with T-splines and Fung-type material models. *Computational Mechanics*, 55:1211–1225, 2015.
133. Y. Bazilevs, V. M. Calo, J. A. Cottrell, J. A. Evans, T. J. R. Hughes, S. Lipton, M. A. Scott, and T. W. Sederberg. Isogeometric analysis using T-splines. *Computer Methods in Applied Mechanics and Engineering*, 199:229–263, 2010.
134. V. L. Huynh, T. Nguyen, H. L. Lam, X. G. Guo, and R. Kafesjian. Cloth-covered stents for tissue heart valves, 2003. US Patent 6,585,766.
135. D. K. Hildebrand. Design and evaluation of a novel pulsatile bioreactor for biologically active heart valves. Master’s thesis, University of Pittsburgh, Pittsburgh, United States, 2003.
136. A. K. S. Iyengar, H. Sugimoto, D. B. Smith, and M. S. Sacks. Dynamic in vitro quantification of bioprosthetic heart valve leaflet motion using structured light projection. *Annals of Biomedical Engineering*, 29(11):963–973, 2001.
137. M. C. H. Wu, D. Kamensky, C. Wang, A. J. Herrema, F. Xu, M. S. Pigazzini, A. Verma, A. L. Marsden, Y. Bazilevs, and M.-C. Hsu. Optimizing fluid–structure interaction systems with immersogeometric analysis and surrogate modeling: Application to a hydraulic arresting gear. *Computer Methods in Applied Mechanics and Engineering*, 316:668–693, 2017.
138. C. Wang, M. C. H. Wu, F. Xu, M.-C. Hsu, and Y. Bazilevs. Modeling of a hydraulic arresting gear using fluid-structure interaction and isogeometric analysis. *Computers & Fluids*, 142:3–14, 2017.
139. D. Kamensky, J. A. Evans, M.-C. Hsu, and Y. Bazilevs. Projection-based stabilization of interface Lagrange multipliers in immersogeometric fluid–thin structure interaction analysis, with application to heart valve modeling. *Computers & Mathematics with Applications*, 74:2068–2088, 2017.
140. Y. Yu, D. Kamensky, M.-C. Hsu, X. Y. Lu, Y. Bazilevs, and T. J. R. Hughes. Error estimates for projection-based dynamic augmented Lagrangian boundary condition enforcement, with application to immersogeometric fluid–structure interaction. *Mathematical Models and Methods in Applied Sciences*, 2018. <https://doi.org/10.1142/S0218202518500537>.
141. H. Casquero, Y. Zhang, C. Bona-Casas, L. Dalcin and H. Gomez. Non-body-fitted fluid–structure interaction: Divergence-conforming B splines, fully-implicit dynamics, and variational formulation. *Journal of Computational Physics*, 2018. <https://doi.org/10.1016/j.jcp.2018.07.020>.
142. H. Casquero, C. Bona-Casas, and H. Gomez. A NURBS-based immersed methodology for fluid–structure interaction. *Computer Methods in Applied Mechanics and Engineering*, 284:943–970, 2015.
143. H. Casquero, L. Liu, C. Bona-Casas, Y. Zhang, and H. Gomez. A hybrid variational-collocation immersed method for fluid–structure interaction using unstructured t-splines. *International Journal for Numerical Methods in Engineering*, 105(11):855–880, 2015.
144. H. Casquero, C. Bona-Casas, and H. Gomez. NURBS-based numerical proxies for red blood cells and circulating tumor cells in microscale blood flow. *Computer Methods in Applied Mechanics and Engineering*, 316:646–667, 2017.
145. A.F. Sarmiento, A.M.A. Côrtes, D.A. Garcia, L. Dalcin, N. Collier, and V.M. Calo. PetIGA-MF: A multi-field high-performance toolbox for structure-preserving B-splines spaces. *Journal of Computational Science*, 18(Supplement C):117–131, 2017.